The Astrophysical Journal, 672:122–137, 2008 January 1

VIRIAL SCALING OF MASSIVE DARK MATTER HALOS: WHY CLUSTERS PREFER A HIGH NORMALIZATION COSMOLOGY

A. E. Evrard,[1,2] J. Bialek,[1] M. Busha,[1] M. White,[2] S. Habib,[3] K. Heitmann,[3] M. Warren,[3] E. Rasia,[1,4,5,6] G. Tormen,[5] L. Moscardini,[4,7] C. Power,[8] A. R. Jenkins,[9] L. Gao,[9] C. S. Frenk,[9] V. Springel,[10] S. D. M. White,[10] and J. Diemand[11,12]

Received 2007 April 2; accepted 2007 June 21

ABSTRACT

We present a precise estimate of the bulk virial scaling relation of halos formed via hierarchical clustering in an ensemble of simulated cold dark matter cosmologies. The result is insensitive to cosmological parameters; the presence of a trace, dissipationless gas component; and numerical resolution down to a limit of ~1000 particles. The dark matter velocity dispersion scales with total mass as $\log[\sigma_{\rm DM}(M,z)] = \log(1082.9 \pm 4.0 \text{ km s}^{-1}) + (0.3361 \pm 0.0026)\log[h(z)M_{200}/10^{15}\ M_\odot]$, with $h(z)$ being the dimensionless Hubble parameter. At fixed mass, the velocity dispersion likelihood is nearly lognormal, with scatter $\sigma_{\ln\sigma} = 0.0426 \pm 0.015$, except for a tail with higher dispersions containing 10% of the population that are merger transients. We combine this relation with the halo mass function in ΛCDM models and show that a low normalization condition, $S_8 = \sigma_8(\Omega_m/0.3)^{0.35} = 0.69$, favored by recent *WMAP* and SDSS analysis requires that galaxy and gas-specific energies in rich clusters be 50% larger than that of the underlying dark matter. Such large energetic biases are in conflict with the current generation of direct simulations of cluster formation. A higher normalization, $S_8 = 0.80$, alleviates this tension and implies that the hot gas fraction within r_{500} is $(0.71 \pm 0.09)\ h_{70}^{-3/2}\ \Omega_b/\Omega_m$, a value consistent with recent Sunyaev-Zel'dovich observations.

Subject headings: cosmology: miscellaneous — cosmology: theory — dark matter — galaxies: clusters: general — gravitation — intergalactic medium

Online material: color figures

1. INTRODUCTION

The emergence of the cosmic web of large-scale structure is a dynamic, hierarchical process. Galactic-scale halos, with formation redshifts greater than 1, exhibit dynamical maturity through the equilibrium nature of the galaxies housed within them. The well-known virial scaling relations—Tully-Fisher for spirals and fundamental plane for ellipticals—are manifestations of advanced dynamical age. The largest halos in the universe, those that harbor groups and clusters of galaxies, assemble at recent epochs and for this reason are widely thought to be much further from dynamical equilibrium.

This point of view is supported by manifold observational evidence for ongoing cluster mergers. Popular examples, such as A754 (Henry et al. 2004) and the well-known "bullet cluster" 1E 0657−56 (Markevitch et al. 2002), show multiple peaks in X-ray emission and galaxy number density (Zabludoff & Zaritsky 1995). In the case of the bullet cluster, weak gravitational lensing reveals multiple peaks in dark matter that trace well the collisionless galaxies but not the hot intracluster gas (Clowe et al. 2006). Similar features are exhibited in beautiful *HST* ACS and *Chandra* images of the bimodal cluster CL 0152−1357 (Jee et al. 2005), where a slight lag in X-ray peaks relative to the dark matter and galaxies is seen. These signatures, along with spatial temperature variations of the sort compiled by Belsole et al. (2005) are consistent with those anticipated by early gas dynamical simulations of merging systems (Evrard 1990; Navarro et al. 1995; Bryan & Norman 1998; Evrard et al. 1996).

On the other hand, empirical evidence supports a seemingly contradictory point of view of clusters as a population of dynamically relaxed systems. Local X-ray flux-limited samples display tight correlations between intracluster gas temperature and a number of other observable features, such as luminosity after core excision (Markevitch 1998; Arnaud & Evrard 1999), isophotal size (Mohr & Evrard 1997), intracluster gas mass (Mohr et al. 1999), thermal Sunyaev-Zel'dovich decrement (Nagai 2006), and galactic content measured at near-infrared (Lin et al. 2004; Lin & Mohr 2004) or red bandpasses (Popesso et al. 2004). The level of intrinsic scatter in these relations is a few tens of percent or less (O'Hara et al. 2006), making these signatures, and derived quantities such as the gas mass fraction (Allen et al. 2004; LaRoque et al. 2006), a foundation for likelihood estimates of cosmological parameters (Voit 2005; Lima & Hu 2005).

These lines of evidence paint clusters as a family of nearly self-similar, dynamically relaxed systems that can be effectively rank-ordered by a single parameter, taken by theorists to be total mass (Kaiser 1986). The assumption of virial equilibrium, which Peebles (1970) showed is rapidly approached after violent collapse

[1] Department of Physics and Michigan Center for Theoretical Physics, University of Michigan, Ann Arbor, MI 48109.
[2] Departments of Physics and Astronomy, University of California, Berkeley, CA 94720.
[3] Los Alamos National Laboratory, Los Alamos, NM 87545.
[4] Dipartimento di Astronomia, Universitá di Bologna, via Ranzani 1, I-40127 Bologna, Italy.
[5] Dipartimento di Astronomia, Universitá di Padova, vicolo dell'Osservatorio 2, I-35122 Padova, Italy.
[6] *Chandra* Fellow.
[7] INFN, National Institute for Nuclear Physics, Sezione di Bologna, viale Berti Pichat 6/2, I-40127 Bologna, Italy.
[8] Centre for Astrophysics and Supercomputing, Swinburne University of Technology, P.O. Box 218, Hawthorn, 3122 Victoria, Australia.
[9] Department of Physics, Durham University, South Road, Durham DH1 3LE, UK.
[10] Max-Planck-Institut für Astrophysik, Karl-Schwarzschild-Strasse 1, D-85740 Garching, Germany.
[11] UCO/Lick Observatory, University of California at Santa Cruz, Santa Cruz, CA 95064.
[12] *Hubble* Fellow.

and which is further validated in this paper, allows gas temperature or galaxy velocity dispersion to serve as observable proxies for total mass.

Recent weak-lensing studies, however, question the regularity of the population by offering evidence for large scatter in the lensing mass-temperature relation. In particular, the subset of morphologically complex clusters follows a relation offset from those of relaxed objects (Smith et al. 2003; Cypriano et al. 2004; Pedersen & Dahle 2007). These studies pose the question of whether the massive cluster population should be considered a bimodal family.

The first section of this paper addresses the fundamental dichotomy posed above by examining the virial relation of massive halos formed in cosmological simulations. As to the essential question of whether clusters are better described as a structurally regular, one-parameter population, or as a significantly bimodal combination of "relaxed" and "unrelaxed" systems, the evidence from our simulations strongly supports the former, with a caveat that $\sim$10% of the population are strongly interacting systems.

All halo finding schemes are challenged by cases in which two or more halos are in the process of merging into one (White 2002). Our approach is to use a consistent, spherical overdensity definition of dark matter halos across a set of computational samples and divide the population into *primary* and *satellite* halos, with the latter being smaller members of spatially overlapping pairs. We show that the population of halos more massive than $10^{14}\ h^{-1}\ M_{\odot}$ is dominated by primary systems with a regular virial relation. The conditional likelihood $p(\sigma_{\rm DM}|M,z)$ is very close to lognormal, with only 4% dispersion in $\ln\sigma_{\rm DM}$ about a robust mean power-law scaling in mass. Satellite halos are a 5%–10% minority of more dynamically active objects, with a virial relation offset to higher velocities and broader than the primary sample.

Independent samples from six cosmological codes give consistent characterizations of the primary virial relation, a testament to the robustness of existing computational algorithms. Combining them provides a percent-level determination of the slope and intercept, and a 5% statistical uncertainty in the lognormal dispersion. The relation is insensitive to cosmological model, epoch, and the presence of a minority content of dissipationless baryons in halos.

In the second part of this paper, we demonstrate the utility of this calibration by combining it with the mass function to predict the space density of dark halos as a function of their mean specific energy. Comparing with observations of the space density as a function of intracluster gas temperature and galaxy velocity dispersion reveals a tension between expectations from current simulations of galaxy and cluster formation and low normalization cosmologies.

In § 2, we present our simulation ensemble and method of analysis. The ensemble consists mainly of *N*-body models of dark matter clustering, which provide large statistical samples of high-mass halos, but we also include some simulations that follow the coupled evolution of dark matter and collisional baryons, as well as two series of runs that investigate effects of numerical resolution. Virial scaling relations are analyzed in § 3, including tests of numerical resolution, redshift evolution, and halo mass definition. We explore implications for cosmology and cluster physics in § 4.

2. COMPUTATIONAL SAMPLE AND ANALYSIS

When virial equilibrium is satisfied, the specific thermal energy of dark matter in a halo of mass M and radius R will scale with its potential energy, GM/R. When mass is defined using a mean interior density condition, then $R \propto M^{1/3}$ and the kinetic energy scales as $M^{2/3}$. In keeping with tradition (Yahil & Vidal 1977), we use a one-dimensional velocity dispersion $\sigma_{\rm DM}$ to express the specific thermal energy in dark matter,

$$\sigma_{\rm DM}^2 = \frac{1}{3N_p}\sum_{i=1}^{N_p}\sum_{j=1}^{3}\left|v_{i,j}-\bar{v}_j\right|^2, \quad (1)$$

where $v_{i,j}$ is the jth component of the physical velocity of halo member i, the index i ranges over the N_p halo members, and $\bar{v}$ is the mean halo velocity constructed from the same N_p members. In this work, halo membership and total mass are defined using a spherical overdensity approach discussed below in § 2.2.

Instead of a classical interpretation of virial equilibrium, expressed as kinetic to potential energy ratio, $T/W = 0.5$, or a boundary-corrected version thereof (Cole & Lacey 1996; Shaw et al. 2006), we stress the utility of the virial theorem as a dimensional tool to connect total mass to specific energies. The dark matter velocity dispersion connects to observable baryonic signatures, namely the galaxy velocity dispersion $\sigma_{\rm gal}$ and ICM X-ray temperature $T_{\rm X}$, through dimensionless ratios presented in § 4.

2.1. *Simulation Ensemble*

We use an ensemble of simulations consisting of *N*-body and gas dynamic models of vacuum energy universes, listed in Table 1, along with *N*-body realizations of other world models given in Table 2. The ΛCDM simulations of Table 1 employ concordance parameters, with matter density $\Omega_m = 0.3$, vacuum energy density $\Omega_\Lambda = 0.7$, and primordial spectral index $n_s = 1$. Values of the Hubble constant and spectrum normalization σ_8 vary across the ensemble, but the virial relation presented below is insensitive to these parameters. References are listed for previously published simulations, others are new to this work.

The models represent the output of six independent simulation codes. Gravitational forces are computed using tree algorithms (HOT, PKDGRAV), tree plus mesh (GADGET, TreePM), or particle-particle, particle-mesh techniques (HYDRA, P3MSPH). HYDRA, HOT, and GADGET are included in the code comparison study of Heitmann et al. (2005), and HOT, HYDRA, and P3MSPH are among the codes benchmarked in the "Santa Barbara cluster" study of Frenk et al. (1999).

Most of the runs are large-volume representations of random regions, but the CP, JD, JB, and RTM entries are resimulations that focus on a single, dominant halo in each run. There are multiple realizations in these sets, producing halos that typically span a factor of 10 in final mass. The exception is the JD resolution series, discussed in § 3.2 below, which models the evolution of the same initial density field with numerical resolution that varies by many orders of magnitude. Overall, the models span a factor of one million in particle mass ($\bar{\rho}L^3/N_p$).

Although the majority of runs are single fluid and collisionless, the JB, MWb, and RTM models follow the evolution of coupled dark matter and a minority (10%–13%) baryonic component. The physical treatment of the baryons in these models is relatively simple, with heating due to shocks but no cooling or star formation processes. The non-ΛCDM simulations of Table 2 include two simulations of an Einstein-deSitter cosmology, $\Omega_m = 1$, an open model with $\Omega_m = 0.3$ and four realizations of a dark energy universe with equation of state parameter $w = -0.8$, two each with primordial spectra $n_s = 1$ and 0.95.

2.2. *Halo Convention*

We use halo lists identified by individual simulators using a common spherical overdensity (SO) halo definition. The approach

TABLE 1
ΛCDM Simulations

Sample	N_p	L (h^{-1} Mpc)	ε (h^{-1} kpc)	Gas?	Code	Ref.	Remarks
HV	1000^3	3000	100	No	HYDRA	1	$z = 0$ and four sky survey outputs
MS	2160^3	500	5	No	GADGET	2	...
MWa	1024^3	500	18	No	TreePM	3	...
J98	256^3	239.5	36	No	HYDRA	4	...
HOTa	256^3	768	100	No	HOT	5	New
HOTb	256^3	384	50	No	HOT	5	New
MB	256^3	200	30	No	GADGET	6	Evolved to $a = 100$
CP	$0.3–1 \times 10^8$	32.5–479	0.06–5	No	GADGET/PKDGRAV	7	23 resimulations
JD	$10^5–10^8$	213	1.3–355	No	PKDGRAV	8	Resolution series, partly new
JB	2×192^{3a}	80–140	20–40	10%	P3MSPH	9	68 resimulations
MWb	2×192^3	150	20	13%	TreePM	10	...
RTM	2×256^{3a}	479	5	10%	GADGET	11	16 resimulated clusters

[a] Effective particle number in high-resolution zone.

References.—(1) Evrard et al. 2002; (2) Springel et al. 2005; (3) White 2002; (4) Jenkins et al. 1998; (5) this work; (6) Busha et al. 2007; (7) Navarro et al. 2004; (8) Diemand et al. 2004b; (9) O'Hara et al. 2006; (10) White et al. 2002; (11) Rasia et al. 2004.

is motivated by a desire to locate hydrostatic regions centered on peaks in the nonlinear density field. The individual methods differ slightly in their approach to centering and to handling spatial overlap of halos, but all employ a consistent definition of mass.

There are slight differences among the models in the treatment of halo centers. In some cases, halo centers are identified using a Lagrangian-smoothed estimate of the local density, derived from the distance to the Nth nearest neighbor, with $N \simeq 10$ (Casertano & Hut 1985). In others, a friends-of-friends (FOF) group finder is run, and the most bound particle defines the halo center.

The mass M_Δ is defined as the total mass within a sphere with mean interior density $3M_\Delta/4\pi r_\Delta^3 = \Delta\rho_c(z)$, where $\rho_c(z)$ the critical density at redshift z. Several values of Δ are in common use, a reflection of the confusion caused by continual accretion and mergers onto halos during hierarchical clustering (Busha et al. 2005).

For most analyses, we employ a fixed critical threshold $\Delta = 200$. In this case, a structurally identical set of halos will have virial scaling

$$\sigma_{\rm DM} \propto [h(z)M_{200}]^{1/3}, \tag{2}$$

where $h(z) = H(z)/100$ km s^{-1} Mpc^{-1} is the normalized Hubble parameter at redshift z.

We also show results at two other commonly used scales with different evolutionary factors. We define M_{200b} as the mass within a sphere encompassing a mean mass density of 200 times the background matter density $\rho_m(z)$. For this background mass, one expects a scaling of the form

$$\sigma_{\rm DM} \propto \left[(1+z)^{3/2}M_{200b}\right]^{1/3}. \tag{3}$$

Finally, analytic solutions for spherical perturbation evolution (Lahav et al. 1991) motivate the use of a variable threshold $\Delta_{\rm var}(z)$ against the critical density. We use the values of Eke et al. (1996), but scale to an asymptotic value of 200, rather than 178 at high redshift (the $\Omega_m = 1$ limit). This implies a present-epoch value $\Delta_{\rm var}(0) = 115$ in a concordance cosmology. Defining $f_{\rm var}(z) = \Delta_{\rm var}(z)/\Delta_{\rm var}(0)$, the expected redshift scaling for the virial relation is

$$\sigma_{\rm DM} \propto \left[f_{\rm var}^{1/2}(z)h(z)M_{\rm var}\right]^{1/3}. \tag{4}$$

Although this scale has typically been referred to as the "virial mass" $M_{\rm vir}$, we employ the label "var" to avoid misinterpretation of this mass as the *unique* scale at which virial equilibrium is satisfied. Cole & Lacey (1996) demonstrated that the virial ratio $2T/W$ is a weak function of radius near the scales discussed here, and Cohn & White (2005) showed that it is also a weak function of redshift in a ΛCDM cosmology. Shaw et al. (2006) examined the pressure-corrected virial ratio,

$$\beta_{\rm vir} = \frac{2T - E_s}{W} + 1, \tag{5}$$

where T is the kinetic energy, W is the gravitational potential energy, and E_s is a boundary pressure term (Chandrasekhar 1961), and found that $\beta_{\rm vir}$ is nearly constant in the range $\Delta \sim 100–500$. The results presented in § 3.3 confirm that tight virial scalings exist across the full range of scales discussed above. We use corresponding notation for the radial sizes of the above mass definitions: r_{200} is the radius that defines M_{200}, r_{200b} defines M_{200b}, and $r_{\rm var}$ defines $M_{\rm var}$.

TABLE 2
Non-ΛCDM N-Body Simulations

Sample	N_p	L (h^{-1} Mpc)	ε (h^{-1} kpc)	Code	Ref.	Remarks
HVτ	1000^3	2000	100	HYDRA	1	$\Omega_m = 1$, $z = 0$ and four sky survey outputs
J98τ	256^3	239.5	36	HYDRA	2	$\Omega_m = 1$
MWc	256^3	256	24	TreePM	...	$\Omega_m = 0.3$
MWd	256^3	200	30	TreePM	...	4 realizations, $\Omega_m = 0.357$, $w = -0.8$, $n_s = 1$, 0.95

References.—(1) Evrard et al. 2002; (2) Jenkins et al. 1998.

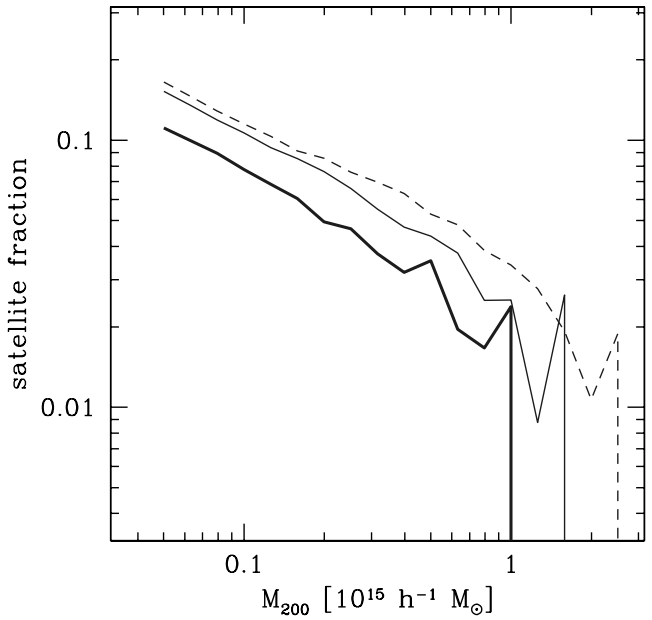

FIG. 1.—Fraction of halos classified as satellites—smaller members of distinct overlapping halo pairs—as a function of mass in the ΛCDM HV model at $z = 0$ (*dashed line*) and in sky surveys extending to $z = 0.54$ (*thin line*) and 1.25 (*thick line*). [*See the electronic edition of the Journal for a color version of this figure*.]

2.3. *Interacting Halos*

Unlike percolation algorithms, which have the virtue of creating exclusive group assignments for simulation particles, the SO algorithm potentially allows a particle to belong to more than one group. The halo finding schemes we employ differ in their treatment of overlapping halos; the scheme used with the HV, J98, and HOT simulations allows it, while the others do not. In all cases, however, an exclusivity condition applies to halo centers; the center of one halo cannot lie inside the spherical boundary of another.

In the cases where overlap is allowed, we label the larger member of an overlapping pair the *primary* halo, and the smaller member the *satellite*. Note that satellites should not be confused with subhalos; the latter are usually subunits lying within a larger halo. The satellites here are merely smaller members of pairs whose spherical volumes intersect. Figure 1 shows the fraction of satellite halos identified in the ΛCDM HV model, the simulation with the largest population of massive halos. At $z = 0$, satellites account for 12% of the population above $10^{14}\ h^{-1}\ M_\odot$. The fraction declines roughly as $M^{-1/2}$ at higher masses. Although more massive systems are more strongly clustered, they are also much rarer, and the latter dominates to make the satellite frequency a decreasing function of mass. Somewhat surprisingly, 3 out of every 100 Coma-sized ($10^{15}\ h^{-1}\ M_\odot$) halos will lie within r_{200} of a more massive neighbor.

Also shown in Figure 1 are satellite fractions for sky survey outputs of the HV simulation that cover 8π steradian of sky to $z = 0.54$ and π steradian to $z = 1.25$ (Evrard et al. 2002). At higher redshift, the more dilute high-mass halos are less likely to overlap. The satellite fraction above $10^{14}\ h^{-1}\ M_\odot$ is 8% for the sky survey extending to $z = 1.25$.

Our estimate of ~10% for the fraction of strongly interacting halos is somewhat higher than the 3.4% derived by Shaw et al. (2006) in their analysis of a computational sample of 2000 well-resolved ($\geq 10^4$ particle) ΛCDM halos more massive than $3 \times 10^{13}\ h^{-1}\ M_\odot$. From their main halo sample, identified with a percolation algorithm (Weller et al. 2005) tuned to $\Delta \simeq 50$, they define a dynamically disturbed, or irregular, subset using a condition on the virial ratio, $\beta_{\rm vir} < -0.2$. Shaw et al. note that the distribution of $\beta_{\rm vir}$ is continuous and that their choice of threshold is motivated by a desire to flag extreme cases. From their Figure 1, it appears that raising the $\beta_{\rm vir}$ threshold to a value -0.15 would roughly double the fraction of irregular halos, bringing it more into line with our estimates based on spatial overlap.

TABLE 3
$\Delta = 200$ PRIMARY HALO VIRIAL RELATION ($N_{15} > 10^4$)

Parameter	Value
Slope, α	0.3361 ± 0.0026
Intercept, $\sigma_{\rm DM,15}$	1082.9 ± 4.0 km s^{-1}
Scatter, $\langle \delta^2_{\ln\sigma} \rangle^{1/2}$	0.0426 ± 0.0015

3. THE VIRIAL RELATION OF DM HALOS

We show that massive dark matter halos adhere to a virial scaling relation of the form

$$\sigma_{\rm DM}(M,z) = \sigma_{\rm DM,15}\left[\frac{h(z)M_{200}}{10^{15}\ M_\odot}\right]^\alpha, \qquad (6)$$

where $\sigma_{\rm DM,15}$ is the normalization at mass $10^{15}\ h^{-1}\ M_\odot$ and α is the logarithmic slope. The final result of this section, derived by combining all well-resolved, ΛCDM samples of primary halos, is a percent-level precision estimate of the fit parameters, $\sigma_{\rm DM,15} = 1082.9 \pm 4.0$ km s^{-1} and $\alpha = 0.3361 \pm 0.0026$. Table 3 lists these parameters along with the standard deviation of $\ln \sigma_{\rm DM}$ about the best-fit relation. We discuss this result in § 3.5.

We begin by establishing agreement among codes for the present-epoch relation in both ΛCDM and non-ΛCDM cosmologies, then move on to test numerical convergence using the JD and CP samples. Time evolution and scale dependence of the virial relation are presented in § 3.3, followed by a brief examination of its future behavior in the deSitter phase of a ΛCDM cosmology, the era of genuine halo equilibrium.

3.1. *Present-Epoch Relation*

Figure 2 shows the virial scalings of the halos in the ensemble of ΛCDM runs at $z = 0$. Each panel shows the internal velocity dispersion, equation (1), for primary halos with mass $M_{200} \geq 10^{14}\ h^{-1}\ M_\odot$. In addition, the HOT, J98, and HV panels also display values for satellite halos, shown as open circles. For clarity, samples with more than 1000 halos are subsampled to that level.

For each model, we perform a least-squares fit to $\log(\sigma_{\rm DM}) = \log(\sigma_{\rm DM,15}) + \alpha \log[h(z)M_{200}/10^{15}\ M_\odot]$ to all primary halos above the $10^{14}\ h^{-1}\ M_\odot$ limit. Although using equal weight per halo puts more emphasis on systems near the mass cutoff, we find that fits to binned versions of the data produce similar results. The least-squares fit for each model is shown by the dashed line in each panel, while the solid line shows the global fit of Table 3.

Best-fit parameters for the primary halo samples are given in Table 4. Also listed is $N_{\rm halo}$, the number of halos above the $10^{14}\ h^{-1}\ M_\odot$ limiting mass, and mass resolution N_{15}, the number of particles in a $10^{15}\ h^{-1}\ M_\odot$ halo. The listed uncertainties are $1\ \sigma$ statistical errors from the least-squares fits.

The ensemble of models covers a wide range in sample size and mass resolution. The Hubble volume (HV) samples contain a half million halos, but the minimum mass limit is resolved by just 45 particles. At the other extreme is the Millennium Simulation sample (MS; Springel et al. 2005) of nearly 2000 halos with

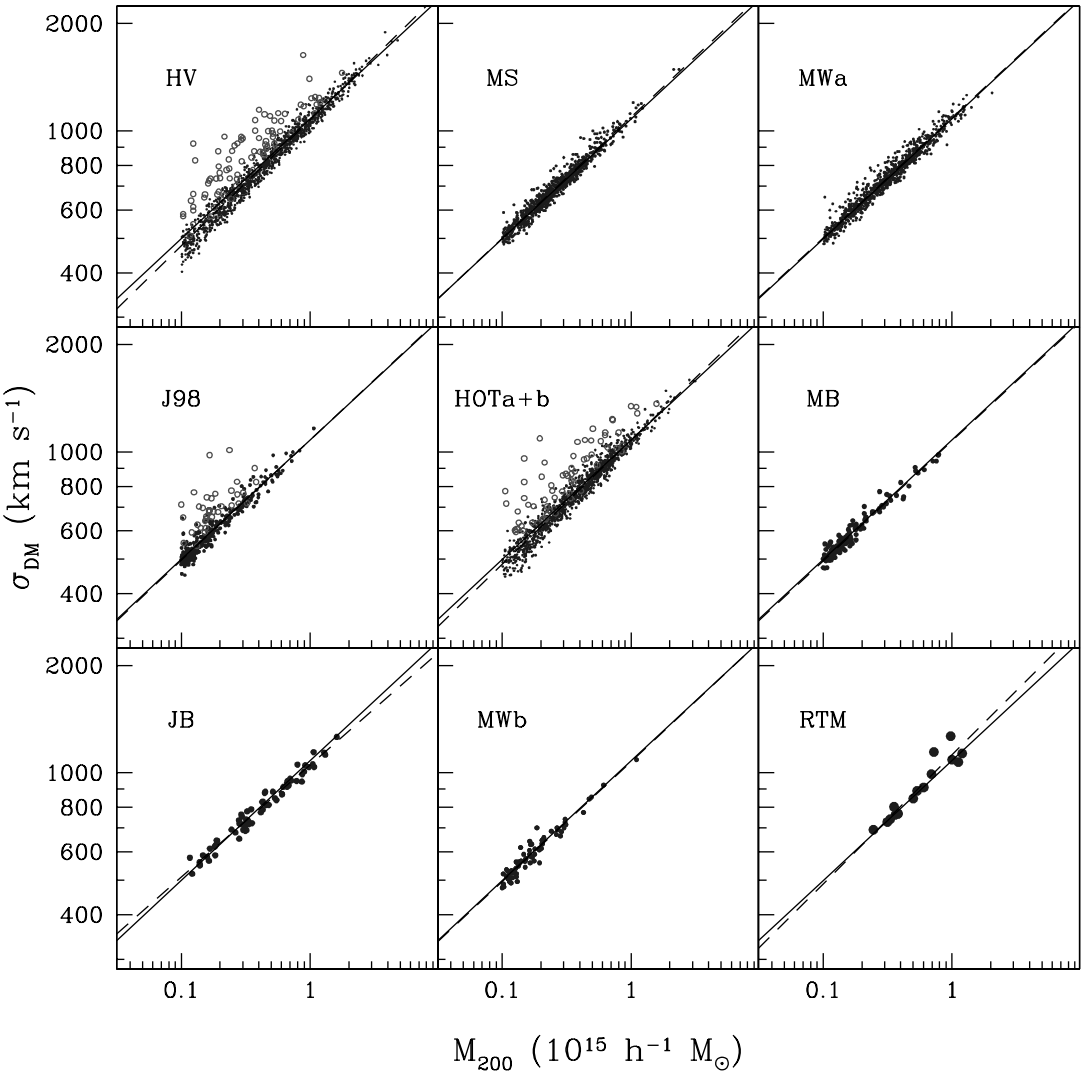

FIG. 2.—Dark matter halo virial relation for ΛCDM models, defined in Table 1, at $z = 0$. Point styles are primary halos (*dots*) and satellites (*open circles*). One thousand randomly chosen halos are shown for samples larger than this size. The top two rows are *N*-body simulations of dark matter; the bottom row includes gas as a second, collisional fluid. The dashed line in each panel is the least-squares fit for that model (Table 4). The solid line in all panels is the global best-fit with parameters listed in Table 3. [*See the electronic edition of the Journal for a color version of this figure.*]

2500 times better mass resolution than HV. In all cases, the primary halo population adheres to a tight relation, with an rms deviation of 4%–5% in $\sigma_{\rm DM}$ at fixed mass. Independent codes produce consistent results for this form.

Models with poor resolution exhibit significantly steeper slopes than those at higher resolution. For example, $\alpha = 0.357 \pm 0.001$ in the HOTa run with $N_{15} = 450$, while $\alpha = 0.335 \pm 0.002$ in the MWa model with 200 times better mass resolution. We show in § 3.2 that this steepening is consistent with the systematic error introduced by numerical resolution at the low-mass limits of the HOTa and HV models. On the other hand, our resolution tests below support the finding that these models have sufficient resolution to accurately measure the intercept at $10^{15}\ h^{-1}\ M_\odot$.

Figure 3 plots the conditional likelihood, $p(\sigma_{\rm DM}|M)$, determined from the residuals about the best-fit power-law relations for the samples of Figure 2. For the low-resolution runs HV and HOTa, we increase the mass limit in this figure to $5 \times 10^{14}\ h^{-1}\ M_\odot$; all other panels remain limited at $10^{14}\ h^{-1}\ M_\odot$.

The velocity dispersion likelihood for primary halos is nearly lognormal with standard deviation $\langle \delta^2_{\ln\sigma} \rangle^{1/2} = 0.04$. There are clear signs of nonzero skewness, particularly in the MS and MWa samples that have the largest number of well-resolved halos. The median values of $\ln(\sigma_{\rm DM})$ are 0.08 and 0.10 times the standard deviations of these samples, and the skewness, $N \sum (x - \bar{x})^3 / [\sum (x - \bar{x})^2]^{3/2}$, is 0.74 ± 0.12 and 0.85 ± 0.08, respectively. The analytic model of Afshordi & Cen (2002) anticipates skewness, but it also predicts that the variance should decline with increasing mass, a feature that is not seen in our data.

The likelihood $p(\sigma_{\rm DM}|M)$ for satellite halos in the HV, HOT, and J98 models is displaced to higher values, by 0.13 in mean $\ln(\sigma_{\rm DM})$, and is broader than the primary population by a factor of 2. These features are consistent with a picture of satellites as merging systems. Since the simple density threshold definition used for halos does not take particle binding energy into account, the satellite systems typically consist of a mixture of some locally bound material along with a hotter component contributed by the neighboring primary. More detailed group-finding treatments, such as those that combine a percolation algorithm with dynamical identification of subhalos (Springel et al. 2001; Weller et al. 2005), will be required to clarify the nature of satellites.

The virial relations of non-ΛCDM models are shown in Figure 4. As in Figure 2, dashed lines are best fits to each model and solid

TABLE 4
$\Delta = 200$ Primary Halo Virial Relation Fits

Sample	$N_{\rm halo}$	N_{15}	$\sigma_{\rm DM,15}$	α	$\langle \delta^2_{\ln\sigma} \rangle^{1/2}$
ΛCDM, present epoch					
HV-z0	23636	450	1073.5 ± 0.5	0.354 ± 0.001	0.0439 ± 0.0002
MS	1938	1162800	1093 ± 4	0.340 ± 0.002	0.0386 ± 0.0006
MWa	4524	103180	1086 ± 3	0.336 ± 0.001	0.0409 ± 0.0006
J98	319	14660	1080 ± 11	0.338 ± 0.006	0.049 ± 0.003
HOTa	427	450	1079 ± 3	0.349 ± 0.007	0.045 ± 0.002
HOTb	1358	3400	1090 ± 5	0.343 ± 0.002	0.045 ± 0.002
MB	133	25190	1072 ± 13	0.336 ± 0.007	0.036 ± 0.004
JB	67	∼15000	1053 ± 8	0.316 ± 0.007	0.037 ± 0.003
MWb	158	∼25000	1075 ± 14	0.337 ± 0.007	0.040 ± 0.003
RTM	16	∼300000	1121 ± 28	0.361 ± 0.032	0.058 ± 0.013
CP	23	$\sim 10^6$	1087 ± 16	0.331 ± 0.002	0.044 ± 0.006
Non-ΛCDM, present epoch					
HVτ-z0	25743	450	1079.5 ± 0.5	0.355 ± 0.001	0.0500 ± 0.0003
J98τ	652	4400	1085 ± 9	0.337 ± 0.004	0.050 ± 0.002
MWc	586	18020	1102 ± 7	0.341 ± 0.004	0.046 ± 0.002
MWd	984	21170	1101 ± 6	0.342 ± 0.003	0.0419 ± 0.0008
ΛCDM, $z > 0$					
HV-ss	20553	450	1077.5 ± 0.7	0.350 ± 0.001	0.0472 ± 0.0002
HVτ-ss	13049	450	1079 ± 1	0.361 ± 0.002	0.0503 ± 0.0002
JB-z1	777	∼15000	1075 ± 3	0.330 ± 0.003	0.045 ± 0.002

Note.—Least-squares fits use equal weight per halo above limiting mass $10^{14}\ h^{-1}\ M_\odot$ ($5 \times 10^{14}\ h^{-1}\ M_\odot$ for HOTa and all HV runs).

lines give the global ΛCDM relation of Table 3. Despite the fact that the assembly history of halos is sensitive to cosmology, the resultant virial relations are remarkably robust. The power-law fits of these models are consistent with that of the ΛCDM family to within a few percent in intercept and slope.

3.2. *Numerical Resolution*

Simulations of random cosmic volumes have the benefit of producing statistical samples of halos that are unbiased in the large volume limit, and can be made so by appropriate mode sampling of finite-volume realizations (Sirko 2005). The principal drawback of this approach is the differential mass resolution imposed by the fixed particle mass; smaller halos are simply composed of fewer particles. The HV and HOTa samples push numerical resolution toward its lowest practical limit ($N_p \geq 45$). On the other hand, constrained initial conditions (Bertschinger 1987) and resimulation techniques (Navarro & White 1994; Tormen et al. 1997) can produce ensembles with fixed resolution across a range of mass scales, but halo sampling under this approach need not be uniform or volume complete.

We find that the resimulation and large volume samples produce consistent normalizations for the virial relation. However, estimates of the slope show sensitivity to numerical resolution. The poorly resolved models, HV and HOTa, have $\alpha \simeq 0.36$, equivalent to a ∼7% reduction in velocity dispersion at $10^{14}\ h^{-1}\ M_\odot$ with fixed $\sigma_{\rm DM,15}$ normalization.

To address whether this reduction in velocity dispersion is to be expected purely from numerical resolution, we turn to the JD ensemble, a resimulation series of a single halo originally used by Diemand et al. (2004b) in a study of inner density profiles. The published work contained high-resolution resimulations. We include here lower resolution realizations that use the same initial perturbations truncated at progressively lower Nyquist frequencies.

Table 5 lists the halo properties of this series. The 12 runs span nearly six decades in mass resolution, with N_{200}, the number of particles within r_{200}, ranging from 33 to 10^7. At lower resolution, the loss of total power in the realized density field delays halo collapse, leading to lower values of the mass M_{200} at $z = 0$. The velocity dispersion also tends to decrease as the resolution degrades. The exception is the realization with $N_{200} = 82$. From visual inspection of the output, this system differs from the others in terms of its dynamical phase. It is experiencing a major merger while systems in the remainder of the series are relatively quiescent.

For each member of the series, we employ $M^{1/3}$ scaling to determine the effective value of the intercept $\sigma_{\rm DM,15}$. The results are listed in Table 5 and are plotted against numerical resolution N_{200} in Figure 5. The inferred velocity dispersion normalization is extremely robust. It lies within ±2% of the highest resolution value until the number of particles within r_{200} falls below ∼500 particles. At the level of 30 particles within r_{200}, the drop in $\sigma_{\rm DM,15}$ has grown to ∼15%, still a modest reduction given the extremely degraded resolution.

For the HV and HOTa simulations, these results suggest an underestimate, at the ∼10% level, in velocity dispersion at $10^{14}\ h^{-1}\ M_\odot$, or 45 particles. At the normalization mass scale of $10^{15}\ h^{-1}\ M_\odot$, the inferred bias should be closer to ∼1%. The differential effect of this bias is consistent with the degree needed to tilt the HV and HOTa relations by ∼0.03 in slope, while leaving the intercept $\sigma_{\rm DM,15}$ little affected.

Determination of the slope α is best done with high-resolution simulations that cover a wide dynamic range in mass. The CP series satisfies this design criterion, covering 5 orders of magnitude in mass with million-particle-per-halo simulations.

The virial relation for the CP series, shown in Figure 6, has a best-fit slope $\alpha = 0.331 \pm 0.002$, a value consistent with the

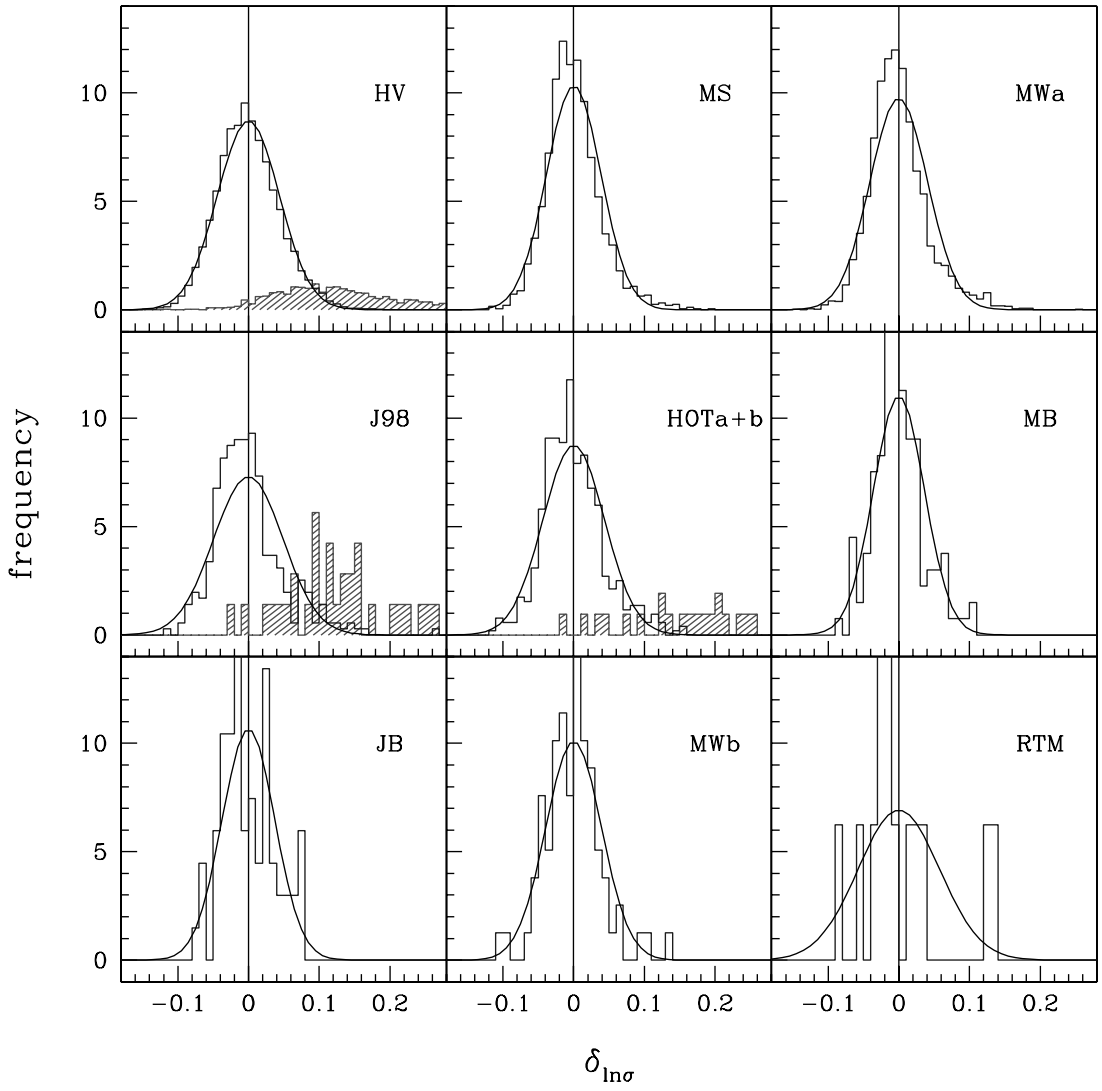

FIG. 3.—Distributions of deviations in $\ln \sigma_{\rm DM}$ about the best-fit relations shown in Fig. 2 for primary (*open histograms*) and satellite halos (*shaded histograms*). The solid curve in each panel is a normal distribution with scatter derived from the primary halos of each model and given in Table 4. The normalization of the satellite distribution is enlarged by a factor of 5 for clarity. A minimum mass of $10^{14}\ h^{-1}\ M_\odot$ is applied, except for the low-resolution models HV and HOTa, for which $5\times10^{14}\ h^{-1}\ M_\odot$ is used. [*See the electronic edition of the Journal for a color version of this figure.*]

self-similar expectation of 1/3. Given the well-documented evidence for departures from self-similarity across the mass spectrum, the 1% agreement in slope is certainly surprising. Compared to cluster-scale halos, those of dwarf galaxies are rounder, more centrally concentrated, and have more isotropic particle orbits (Prada et al. 2006). Despite these differences, the self-similar form of the virial relation is respected across the range 10^{10}–$10^{15}\ h^{-1}\ M_\odot$. The intercept and scatter in $\sigma_{\rm DM}$ are consistent with the ensemble values (see Table 4).

3.3. *Evolution and Mass Measure*

The preceding analysis establishes a well-defined virial relation for massive halos at the present epoch. We now address how this relation evolves in time. Along with the default M_{200} measure, we also examine the evolution based on the other mass scales discussed in § 2.2.

Figure 7 shows the virial relation for halos sampled in the redshift range $z = 0$ to 1.5. The data include sky survey samples from HV models of ΛCDM and τCDM cosmologies, along with samples at 12 discrete redshifts from gas dynamic simulations of ΛCDM clusters. Fits to these data are given in Table 4.

In all three cases, the virial relation scales according to the expectation of equation (2). By virtue of offering a low-dispersion estimator of the potential well depth, $\sigma_{\rm DM}$, one might argue that the measure $h(z)M_{200}$ deserves consideration as the "virial mass" of a halo.

On the other hand, the regularity of halo structure implies that this scaling relation is not unique. In Figure 8, we compare virial relations for the three mass measures discussed in § 2.2. For this exercise, we use a single halo sample taken from the one of the deep octant sky survey outputs of the ΛCDM HV simulation (the NO sample). We employ a mass limit $3\times10^{14}\ h^{-1}\ M_\odot$ as a compromise between sample size and numerical resolution. Fits to the data are listed in Table 6.

The mass measures sample regions of differing radial extent, with M_{200} the innermost and M_{200b} the outermost scales. The virial relation intercept drops at larger radii, a reflection of our choice of normalization at a fixed mass of $10^{15}\ h^{-1}\ M_\odot$ and of the declining velocity dispersion profiles in individual halos beyond the scale radius r_s (Navarro et al. 1997). The slope α, although biased high due to resolution effects discussed above, is consistent for all three mass measures.

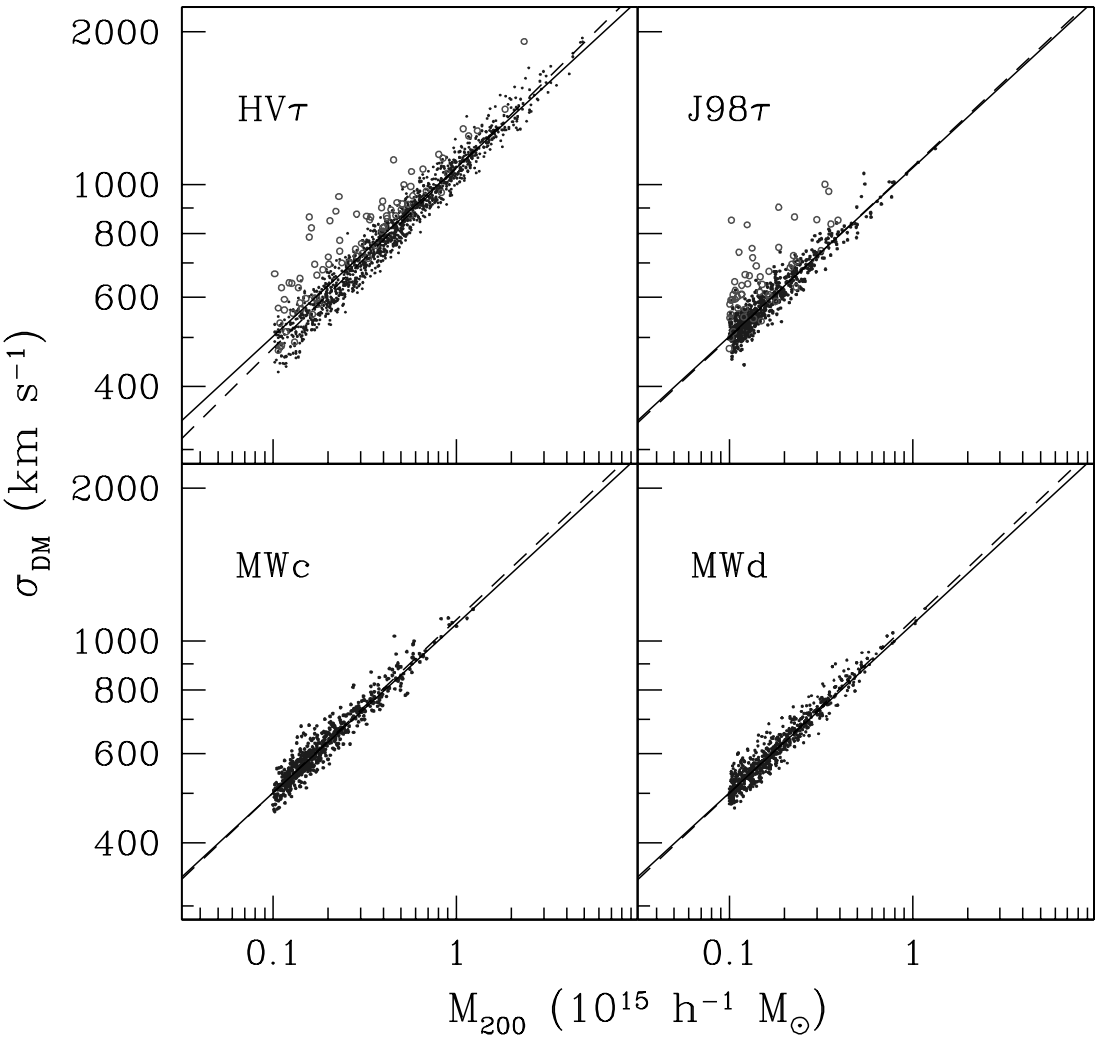

FIG. 4.—The $z = 0$ virial relations of the non-ΛCDM models listed in Table 2. Point and line styles are the same as Fig. 2. Fit parameters for primary halo samples are given in Table 4. [*See the electronic edition of the Journal for a color version of this figure*.]

The fractional scatter in the likelihood $p(\sigma_{\rm DM}|M,z)$ grows slowly as the radial scale is increased, from 0.0487 at M_{200} to 0.0559 at M_{200b}. Jackknife errors in the scatter are 0.0005, implying that the small change in scatter is significant. The longer dynamical times in the outer portions of halos is the likely cause of the increasing variance.

TABLE 5
JD RESOLUTION SERIES

N_{200}	M_{200} (10^{15} h^{-1} $M_\odot$)	$\sigma_{\rm DM}$ (km s^{-1})	$\sigma_{\rm DM,15}$ (km s^{-1})
10519395.....	0.159	601	1108
4756791.....	0.171	619	1114
1386543.....	0.168	608	1101
1362015.....	0.165	606	1104
158962.....	0.154	581	1083
5806.....	0.152	575	1077
698.....	0.146	582	1105
220.....	0.155	550	1023
193.....	0.137	513	995
82.....	0.137	573	1113
34.....	0.112	461	956
33.....	0.107	453	953

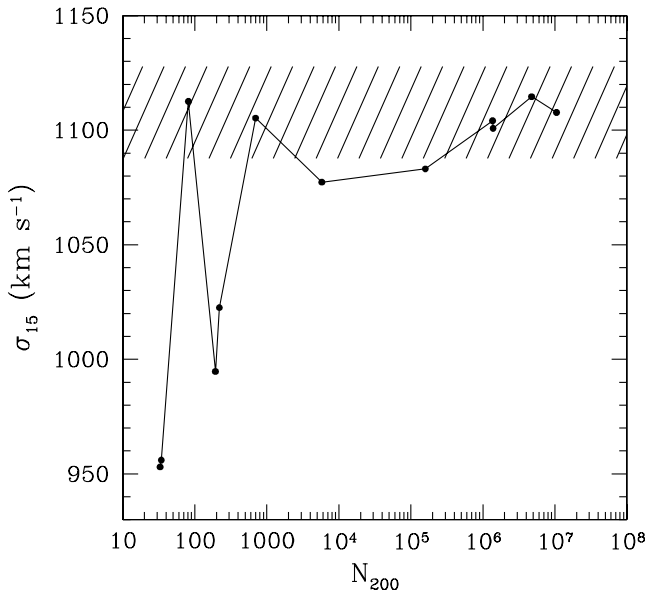

FIG. 5.—Inferred virial relation normalization as a function of number of particles within r_{200} for the JD resolution series of a single halo. The shaded region denotes a 2% range centered on the highest resolution value.

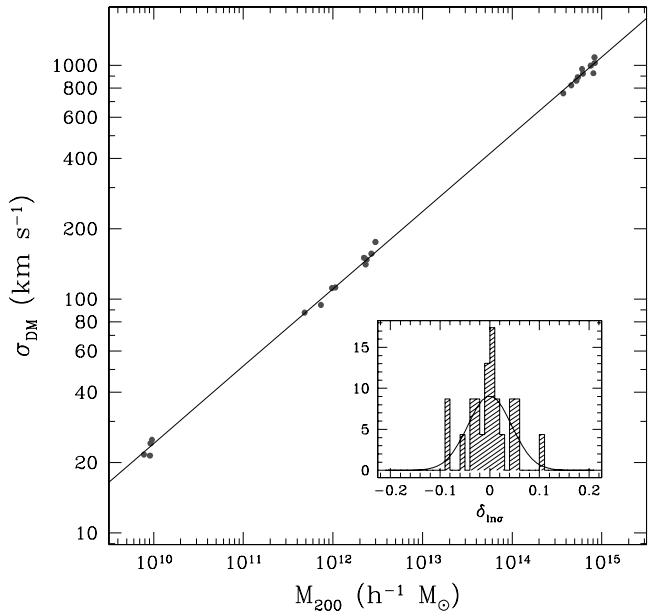

FIG. 6.—Virial scaling for the CP set of 23 very high resolution halos spanning dwarf galaxy to cluster mass scales. The solid line shows the best-fit power law, and the inset shows residuals about the fit. [*See the electronic edition of the Journal for a color version of this figure.*]

The trend of decreasing variance at smaller scales is unlikely to continue to the core regions, $r \lesssim 0.1 r_{200}$. At such small radii, the influence of minor mergers and subhalo transits can be large, and the variance is therefore likely to increase. The HV-z0 sample at $\Delta = 500$ has scatter 0.042, slightly smaller than the 0.0439 value at $\Delta = 200$. This evidence suggests that the minimum variance scale the virial relation lies within the $\Delta = 500$ critical surface.

3.4. *Asymptotic Behavior in the ΛCDM Case*

As a final comment on evolution, we use the MB run (Busha et al. 2007) to explore the behavior of the virial relation in the future of a ΛCDM cosmology. We examine the behavior at scale factor $a/a_0 = 100$, 53 h^{-1} Gyr into the future, and well into the deSitter phase of the vacuum-dominated era when linear growth of large-scale structure has shut down. The physical scale of the cosmic web is exponentially stretched, and the embedded, nonlinear halos evolve in increasing isolation (Nagamine & Loeb 2003). In short, the web has condensed into a spray of isolated halo droplets.

At the present epoch, the ensemble-averaged, radial phase-space structure of halos has two zero velocity surfaces: an inner hydrostatic radius and an outer turnaround radius. Within the wide mixing zone between them lie the mass scales discussed in § 2.2. In the near future of a ΛCDM universe, the hydrostatic surface grows and merges with the turnaround radius, creating a single, well-defined cluster edge (Busha et al. 2005) near the classical turnaround radius defined by critical density contrast $\Delta \simeq 6$ (Gunn & Gott 1972; Peebles 1980).

Figure 9 shows that the $a = 100$ relation is a slightly lowered and substantially tighter version of its present-day counterpart. The intercept, $\sigma_{DM,15} = (1053 \pm 6)$ km s^{-1}, is 3% lower than the present-epoch relation for this simulation, shown in Figure 2. The lowering results from the loss of a small fraction of unbound mass that occurs as accretion ceases (Busha et al. 2005).

The scatter in $p(\sigma_{DM}|M)$ is $1.9\% \pm 0.1\%$ at $a = 100$, meaning the variance has fallen by more than a factor of 4 compared to the present epoch. The variance today must therefore be dominated by transient phenomena associated with accretion and mergers, not by long-lived structural differences, such as variations in halo shape or concentration. Such structural differences persist into the near future.

3.5. *Calibration Summary*

The virial scaling parameters for primary halos, shown in Figures 2, 4, 6, and 7, are summarized in Table 4. Figure 10 shows the dependence of the fit parameters on the degree of numerical resolution, characterized by the N_{15}, the number of particles within a 10^{15} h^{-1} $M_\odot$ halo. The slope and, to a lesser extent, the scatter are biased high in the lowest resolution simulations, but converge for $N_{15} \gtrsim 10^4$, or 1000 particles at the 10^{14} h^{-1} $M_\odot$ limiting mass. The intercept $\sigma_{DM,15}$ shows little sensitivity to resolution.

The high degree of consistency among the models motivates us to combine them to produce an overall fit. We do so using a bootstrap approach on the ΛCDM models of Table 4 with resolution $N_{15} > 10^4$. We make one adjustment to the normalization error, based on the recognition that computational sources—force anisotropies and time integration error in the *N*-body algorithms—will produce a floor in $\sigma_{DM,15}$ uncertainty. For modern algorithms, typical errors in kinetic energy are at the level of 0.5% (Efstathiou et al. 1985). We therefore add a fixed 0.25% fractional error in

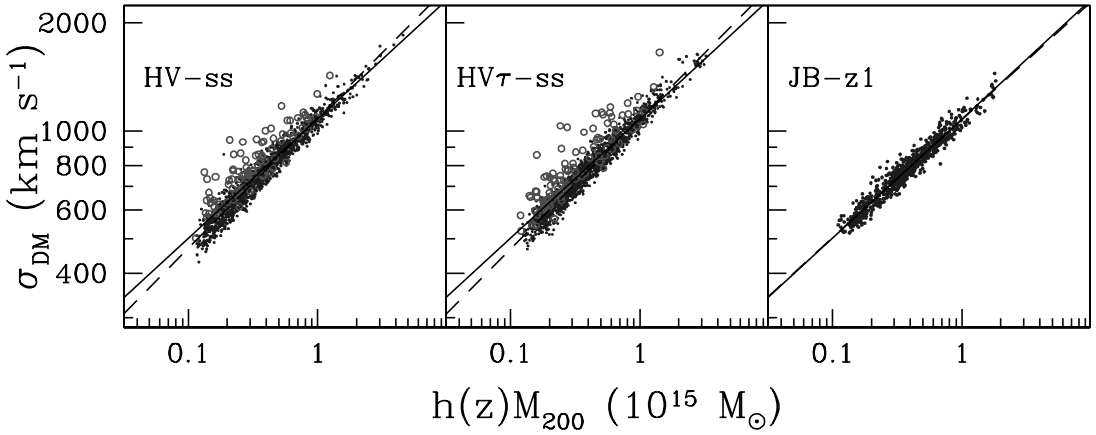

FIG. 7.—Halo virial relation at nonzero redshift for the models indicated. Point and line styles are the same as Fig. 2. The HV models are continuously sampled along light cones extending to $z \simeq 1.5$, while the JB runs are sampled at twelve epochs, spaced equally in time, with $z \leq 1$. [*See the electronic edition of the Journal for a color version of this figure.*]

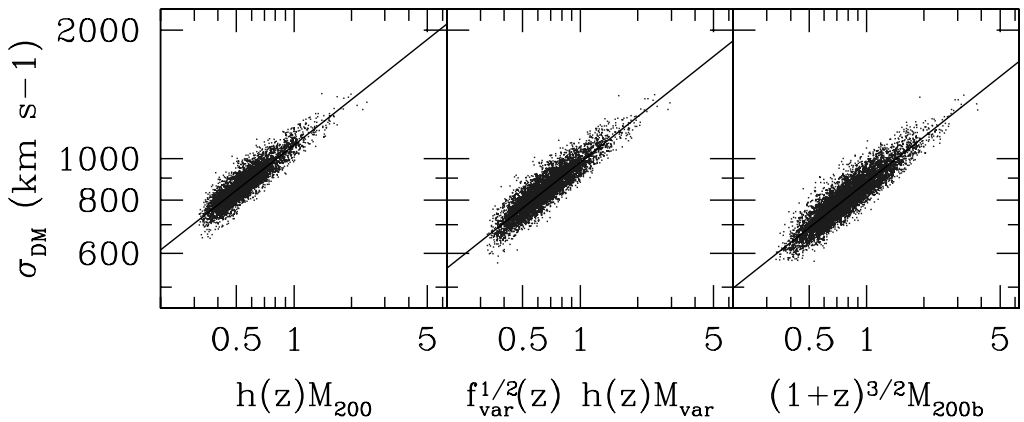

FIG. 8.—Virial relation of primary halos in the HV-NO sky survey sample, with masses defined by (*left to right*) fixed critical, variable, and fixed background density thresholds. The appropriate prefactors of mass are described in § 2.2. [*See the electronic edition of the Journal for a color version of this figure.*]

quadrature to the statistical uncertainties in $\sigma_{DM,15}$. Our bootstrap approach generates a large number of trials, each realizing a random selection of fit parameters assuming Gaussian errors. We then quote the mean and standard error determined from the trial distributions.

The resultant global values, quoted above in Table 3, are shown by the bold lines in Figure 10, and shaded regions show 90% confidence errors. The slope and intercept are determined to better than one percent precision; the uncertainty in the intrinsic variance $\langle \delta^2_{\ln \sigma} \rangle$ is slightly less than 10%.

The global fit values are robust to the choice of N_{15} threshold. Including the less well-resolved models in the fit raises the slope to 0.3393, while the intercept and dispersion change by less than 1 σ. To the extents probed by the simulation ensemble, the fit values are insensitive to cosmological model, epoch, the presence of a trace baryonic component, and the computational algorithm used in the simulation.

The uncertainties in the virial fits are driven by statistical errors. A concerted effort among computing consortia to federate large ensembles of moderate- to high-resolution simulations could readily push statistical errors in $\sigma_{DM,15}$ below the level of current algorithmic accuracy. This eventuality would drive a need for an improved understanding of energy conservation in existing algorithms, potentially stimulating the development of higher accuracy cosmological codes. In § 4, we use the percent-level accuracy in the virial relation as an anchor for the observable specific energies in rich clusters.

4. IMPLICATIONS

The virial relation establishes a strong connection between mass and specific kinetic energy in dark matter. Since experimental detection of dark matter remains elusive even in our own galaxy (Ellis et al. 2005), direct measurement of these velocities is currently out of the question. However, the dark matter potential well depth sets the scale for baryonic physics, and we consider here simple parameterizations for the X-ray temperature, the galaxy velocity dispersion, and the ICM mass fraction.

TABLE 6
VIRIAL RELATION FOR ALTERNATE MASS MEASURES

Mass	N_{halo}	α	$\sigma_{DM,15}$ (km s^{-1})	$\langle \delta^2_{\ln \sigma} \rangle^{1/2}$
M_{200}	4175	0.352 ± 0.003	1080 ± 2	0.0487 ± 0.0005
M_{var}	5308	0.355 ± 0.002	982 ± 1	0.0527 ± 0.0005
M_{200b}	6363	0.355 ± 0.002	880 ± 1	0.0559 ± 0.0005

NOTE.—Derived from HV-NO sky survey samples, mass limited at 3×10^{14} h^{-1} $M_\odot$ in each measure.

4.1. *ICM and Galaxy Components*

The mix of baryonic phases in halos is a complex function of time and halo mass, driven by competing, nonlinear cooling and heating processes. Rich clusters have an advantage in that they represent regions of accelerated galactic development (Bower 1991; Kauffmann et al. 1993). Compared to a typical region in the field, star and massive black hole formation play out at earlier cosmic times in protocluster regions (Springel et al. 2005). This, along with the reduction in cooling rates caused by a growing virial temperature, allows heating to dominate cooling early on, resulting in a low galaxy formation efficiency (Pearce et al. 1999). The baryonic content of rich clusters is thus observed to be only 10%–15% stars and cold ($T \leq 10^5$ K) gas (White et al.

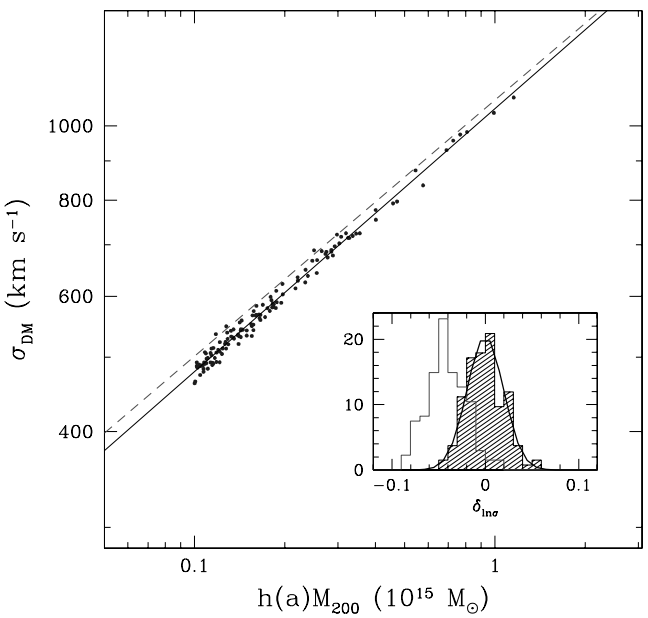

FIG. 9.—Future virial relation of an ΛCDM cosmology. Points show halos at $a \simeq 100$, and the solid line gives the best fit power-law relation. The dashed line shows the relation at $a \leq 1$. The inset gives deviations about the best fit (*shaded histogram*) and the present-epoch (*unshaded histogram*) relations. Loss of unbound material leads to lower velocity dispersions and dynamical relaxation decreases the scatter in velocity dispersion to below 2%. [*See the electronic edition of the Journal for a color version of this figure.*]

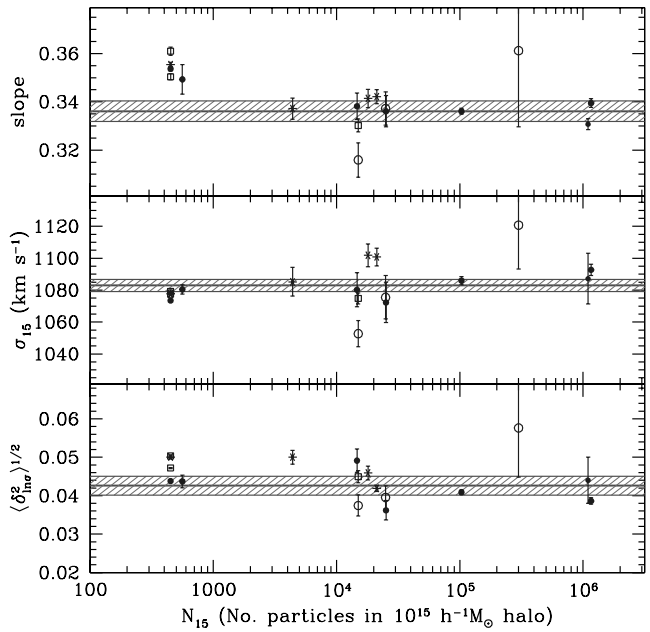

FIG. 10.—Resolution dependence of the primary halo fit parameters for the ΛCDM $z = 0$ data without/with gas (*filled/open circles*), ΛCDM $z > 0$ data (*open squares*), and non-ΛCDM models (*asterisks*). The bold horizontal line and shaded region in each panel are global means and 90% confidence uncertainties for the ΛCDM models determined from bootstrap resampling. [*See the electronic edition of the Journal for a color version of this figure.*]

1993; Ettori 2003). Recent studies that include a diffuse light contribution emphasize the mass dependence of this fraction; stars and hot gas are comparable mass components at $M_{200} = 10^{14} h^{-1} M_\odot$ (Gonzalez et al. 2007).

The mean halo ICM mass fraction within r_Δ will differ from the global baryon fraction Ω_b/Ω_m, due partly to the mass in cold gas and stars but also to differences in the radial structure of the dark matter, ICM, and galaxy components. We parameterize these effects separately.

We first introduce the mean halo baryon bias:

$$\Upsilon \equiv \frac{M_b/M_\Delta}{\Omega_b/\Omega_m}, \tag{7}$$

where M_b is the baryon mass within r_Δ. In addition, we introduce the baryonic ICM mass fraction within r_Δ:

$$\hat{f}_{\rm ICM} = \frac{M_{\rm ICM}}{M_b}. \tag{8}$$

With these definitions, we can relate the local ICM mass fraction to the global baryon fraction

$$f_{\rm ICM} \equiv \frac{M_{\rm ICM}}{M_\Delta} = \hat{f}_{\rm ICM} \Upsilon \left(\frac{\Omega_b}{\Omega_m} \right). \tag{9}$$

To describe baryon energetics, we introduce dimensionless specific energy ratios that enable connections to optical and X-ray observations. Let

$$b_v \equiv \frac{\sigma_{\rm gal}}{\sigma_{\rm DM}} \tag{10}$$

be the ratio of galaxy velocity dispersion to that of the dark matter, also known as the *velocity bias* (Carlberg et al. 1990; Evrard et al. 1994; Colín et al. 2000; Springel et al. 2001; Faltenbacher et al. 2005; Faltenbacher & Diemand 2006). The unbiased case, $b_v = 1$, is expected if both dark matter and galaxies behave as collisionless fluids, and if the galaxies fairly sample the mass-weighted phase structure of the dark matter.

The velocity structure of clusters is sensitive to galaxy type, with late types having roughly 10% higher $\sigma_{\rm gal}$ than early types (Sodre et al. 1989; de Theije & Katgert 1999) and the brightest galaxies having substantially lower dispersions (Biviano et al. 1992). We do not address these detailed dependencies in this paper, but consider only the velocity dispersion of magnitude-limited samples.

For the hot gas, we use the specific, thermal energy defined by the X-ray temperature $T_{\rm X}$ to form the ratio

$$b_T^2 \equiv \frac{kT_{\rm X}/\mu m_p}{\sigma^2_{\rm DM}}, \tag{11}$$

where μ is the mean molecular weight and m_p is the proton mass. Note that b_T^2 is the inverse of the classical β parameter (Cavaliere & Fusco-Femiano 1976). That work envisioned a potential well dominated by the mass in galaxies, so their original measure is now better known as the *spectroscopic beta* parameter:

$$\beta_{\rm spec} \equiv \frac{\sigma^2_{\rm gal}}{kT_{\rm X}/\mu m_p} = \frac{b_v^2}{b_T^2}. \tag{12}$$

This quantity has the benefit of being directly observable. From a heterogeneous sample of 109 clusters, Xue & Wu (2000) found a mean value $\beta_{\rm spec} = 1.0$ at $kT_{\rm X} = 6$ keV.

4.2. *Direct Simulation Constraints*

Direct simulations of the ICM and galaxy components provide independent estimates of the above measures. Two signatures exhibited by early simulations (Evrard 1990; Navarro et al. 1995) have remained robust, even as resolution has increased and new modeling algorithms have emerged. One is that the hot ICM is not completely thermalized. Within r_{200}, kinetic pressure in ordered and turbulent flows contributes 10%–15% relative to thermal pressure. The second is that, under purely gravitational evolution, the local baryon fraction within this scale is slightly depleted relative to the global value.

The "Santa Barbara Cluster" comparison study (Frenk et al. 1999) applies twelve gas dynamics codes to the study of a single cluster realization. The codes agree that the ICM is not completely thermalized in the evolving potential. The resultant mean specific thermal energy of the gas within r_{200} is

$$\langle b_T^2 \rangle_{\rm sim} = (0.87 \pm 0.04) \langle T_{\rm X}/T_m \rangle. \tag{13}$$

The quoted error is the standard deviation among the different codes,[13] and the term in brackets arises because the simulations employ a mass-weighted temperature T_m, while the definition of b_T^2 is with respect to spectroscopic temperature measured by X-ray observations. We employ below a value $\langle T_{\rm X}/T_m \rangle = 1.10 \pm 0.05$ measured within r_{500} by Nagai et al. (2006) using detailed mock *Chandra* observations of simulated clusters.

The Santa Barbara solutions also provide an estimate of the halo baryon bias, $\Upsilon = 0.86 \pm 0.06$. Pearce et al. (1994) offered evidence that the depletion arises from energy transfer into the ICM from the dark matter during major mergers. Recent ART and

[13] Excluding the lowest resolution model that had only a few hundred volumetric cells within the cluster (see Frenk et al. 1999).

GADGET simulations (Kravtsov et al. 2005) found values consistent with this estimate when no gas cooling is allowed, but models with cooling and star formation tend to be overabundant in baryons, $\Upsilon \simeq 1.05$ at r_{500}. Note that these simulations do not include the effects of AGN feedback.

The fraction of baryons that condense into stars and cold gas is difficult to model accurately. Ettori et al. (2006) analyzed the 480^3 particle GADGET models of Borgani et al. (2004) plus additional resimulations and found that, while the overall baryon fraction within r_{200} is relatively robust, $\Upsilon = 0.94 \pm 0.03$, the hot gas fraction $\hat{f}_{\rm ICM}$ is sensitive to physical treatment, varying by 40% over the range of treatments studied. The ART models of Kravtsov et al. (2005) exhibit low values $\hat{f}_{\rm ICM} = 0.58 \pm 0.08$, but most (8 out of 9) of their halos are group-scale systems with $kT < 3$ keV.

Given the degree of uncertainty in the current generation of simulations, we quote only a weak constraint on the halo ICM fraction

$$\left\langle \hat{f}_{\rm ICM} \Upsilon \right\rangle_{\rm sim} = 0.80 \pm 0.15. \quad (14)$$

Note that the 1 σ range nearly allows for the hot phase baryon fraction to identically match the global value. In the outer parts of clusters, the scale dependence of the hot gas fraction is weak, and we assume the above to hold over the range $\Delta \sim 200$–500.

The galaxy velocity bias determined by direct simulation is a subject of active investigation. By identifying galaxies with subhalos in a high-resolution N-body simulation, Colín et al. (2000) found $b_v = 1.2$–1.3, a result that conflicted with early gas dynamic simulations that indicated $b_v < 1$. Diemand et al. (2004a) pointed out that subhalo populations in clusters are very close to stationary solutions of the Jeans equation. The massive subhalo population with significant velocity bias is therefore more extended than the dark matter, and is in conflict with the observed number density profiles of cluster galaxies.

Gao et al. (2004) showed that galaxy populations whose formation and evolution are followed within high-resolution dark matter simulations using the semianalytic approach pioneered by Springel et al. (2001) can match the observed galaxy density profiles of clusters well and, as a result, have smaller kinematic bias. Figure 11 gives the ratio of galaxy to dark matter velocity dispersion for all halos in the Millennium Simulation more massive than $10^{14}\ h^{-1}\ M_\odot$. Results are shown at redshifts $z = 0$ and 1, and for all galaxies with absolute B-band absolute magnitudes $M_B < -17$. The galaxy catalogs used here are based on the galaxy formation model of De Lucia & Blaizot (2007), which gives good fits to the observed field and cluster luminosity functions and to the masses of observed central cluster galaxies, as well as fitting the observed galaxy number density profiles of clusters. The mean velocity bias changes from being slightly less than unity at high redshift, $\langle b_v \rangle = 0.959 \pm 0.002$, to slightly above one at the present epoch, $\langle b_v \rangle = 1.037 \pm 0.001$.

Faltenbacher & Diemand (2006) showed that an alternative approach of mapping galaxy luminosity to subhalo size at the time of accretion (Nagai & Kravtsov 2005; Conroy et al. 2006) yields a similarly weak velocity bias, $b_v = 1.02$, within $r_{\rm var}$. Biviano et al. (2006) analyzed virial mass estimates using the gas dynamic simulations of Borgani et al. (2004) and found a small, negative effect, $b_v = 0.95$.

In short, the latest simulations that use either physically motivated subhalo models or a direct approach to baryon cooling and star formation indicate that the velocity bias is likely to be small. We summarize the current situation as

$$\langle b_v \rangle_{\rm sim} = 1.00 \pm 0.05. \quad (15)$$

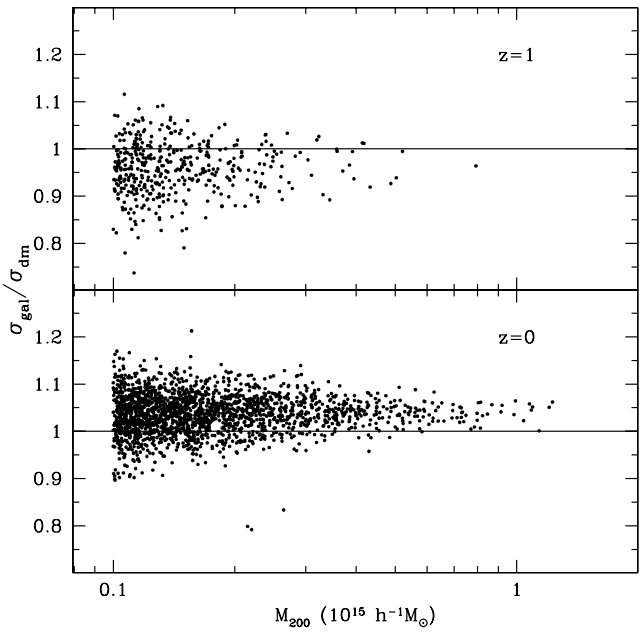

FIG. 11.—Ratio of galaxy to dark matter velocity dispersion within r_{200} for galaxies with absolute magnitudes $M_B < -17$ in the catalogs produced for the Millennium Simulation by De Lucia & Blaizot (2007). Results are shown for all halos more massive than $10^{14}\ h^{-1}\ M_\odot$ at $z = 1$ (*top*) and $z = 0$ (*bottom*).

4.3. *Cluster Space Densities, Gas Fractions, and the Power Spectrum Normalization*

The space density of clusters hotter than 6 keV and lying within $z = 0.09$ is observed to be $10^{-6.5\pm0.2}\ h^3$ Mpc^{-3} (Ikebe et al. 2002; Henry 2004). This observation sparked a flurry of activity focused on determining the power spectrum normalization σ_8 (see, e.g., Table 5 of Henry 2004). Over the years, published values tended to vary by many times their statistical uncertainties. The systematic variation was driven partly by different statistical treatments and partly by differences in the assumed mass-temperature relation (Pierpaoli et al. 2003). Mass normalization uncertainty introduces error in the power spectrum normalization, $\delta(\ln \sigma_8) \simeq 0.4\delta(\ln M)$ (Evrard et al. 2002; Huterer & White 2002).

We now revisit this issue from the inverse perspective. We aim to derive the mass-temperature normalization, or the equivalent b_T^2, required to match the observations.

The halo space density is now well characterized as a function of the spatially filtered, linear matter power spectrum (Sheth & Tormen 1999; Jenkins et al. 2001; Reed et al. 2007; Warren et al. 2006). For massive clusters, the normalization σ_8 and matter density parameter Ω_m control the space density via the combination

$$S_8 = \sigma_8 (\Omega_m / 0.3)^{0.35}. \quad (16)$$

This feature is demonstrated in Figure 12. Instead of mass as the independent variable, we plot the cumulative space density as a function of potential well depth $\sigma_{\rm DM}^2$, determined by convolving the M_{200} mass function with the dark matter virial relation determined above.

The three line styles show matter densities $\Omega_m = 0.24$, 0.30, and 0.36, using mass function parameters expressed as linear functions of Ω_m (Evrard et al. 2002). The high normalization, $S_8 = 0.90$, is appropriate for a concordance cosmology (Bahcall et al. 1999), while the low value, $S_8 = 0.69$, is based on the recent *WMAP*3+SDSS analysis of Tegmark et al. (2007), who found $\Omega_m = 0.239 \pm 0.018$ and $\sigma_8 = 0.756 \pm 0.035$.

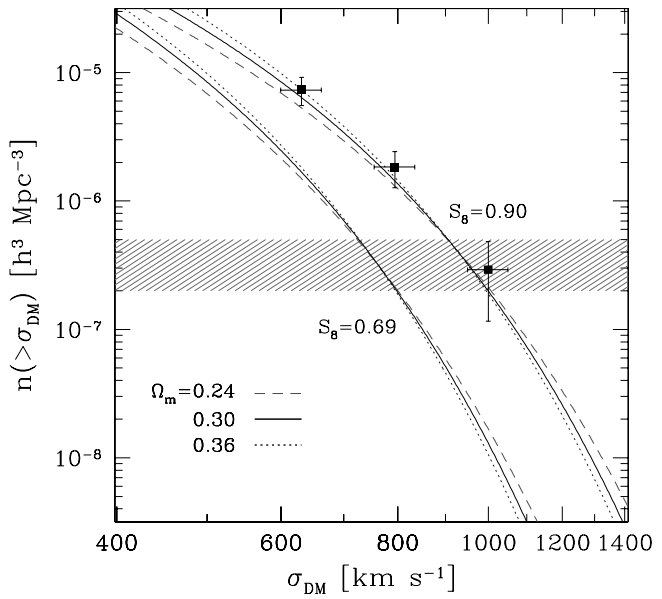

FIG. 12.—Cumulative space density of halos as a function of dark matter velocity dispersion within r_{200}, calculated at $z = 0.06$ for two values of $S_8 = \sigma_8(\Omega_m/0.3)^{0.35}$ listed. The predictions result from convolving the virial scaling, eq. (6) and Table 3, with the Jenkins mass function calibrated for M_{200} (Evrard et al. 2002) using model parameters appropriate for $\Omega_m = 0.24$ (*dashed line*), 0.30 (*solid line*), and 0.36 (*dotted line*). The shaded region shows the observed, local space density of clusters with X-ray temperature greater than 6 keV (Ikebe et al. 2002; Henry 2004). Solid squares with error bars show the space density of CIRS clusters as a function of galaxy velocity dispersion (Rines et al. 2006), with horizontal error bars showing the effect of a ±5% velocity bias. [*See the electronic edition of the Journal for a color version of this figure.*]

The fixed S_8 condition sets the velocity dispersion, or halo mass, at which the cumulative halo space density matches the observed space density of 6 keV clusters. Assuming $\beta_{\rm spec} = 1$, the 6 keV threshold is equivalent to velocity dispersion $\sigma_{\rm gal} = 988$ km s^{-1}. The filled squares in Figure 12 are estimates of the cluster space density as a function of galaxy velocity dispersion from the CIRS sample (Rines et al. 2006).

The CIRS combines local X-ray–selected cluster locations with the SDSS spectroscopic galaxy sample, which is 93% complete within the SDSS sky area for galaxies with *r*-band magnitudes brighter than $r = 17.77$. Velocity dispersions are measured within values of r_{200} estimated directly from the sample virial masses. The space density is determined from 72 clusters in a volume-limited sample within $z = 0.10$. Note that the number density above 1000 km s^{-1} agrees well with the 6 keV X-ray abundance, implying mean $\beta_{\rm spec} = 1$.

Although there are likely to be additional biases due to projection and the specific *r*-band galaxy selection, we do not attempt to model these separately here, and the inferred measures of b_v for CIRS must be interpreted as incorporating these effects. Recent work on mock SDSS cluster samples defined by a `maxbcg` algorithm (Koester et al. 2007) suggests that the line-of-sight dispersion may be ∼10% low compared to $\sigma_{\rm gal}$ of the best-match contributing halo (Becker et al. 2007), implying an effective value of $b_v = 0.9$. However, Biviano et al. (2006) saw a smaller effect using hydrodynamic simulations of galaxy formation. The implications for CIRS are unclear without targeted modeling that tests for sensitivity to details such as cluster selection method, choice of radial scale, redshift, and richness.

Figure 12 shows that the CIRS data follow the high S_8 predictions if the overall bias in galaxy velocity dispersion is small, $b_v = 1$. The low normalization models require a substantial velocity bias $b_v = 1.25$. The recent direct simulations discussed above do not admit such a large effect. The horizontal error bars in Figure 12 reflect the estimate of the theoretical uncertainty quoted in equation (15). Galaxy velocities need to be substantially enhanced to allow the low S_8 normalization. An effect of this magnitude appears unlikely from line-of-sight projection effects alone (Biviano et al. 2006; Becker et al. 2007).

For the X-ray observations, the gas thermal energy parameter b_T^2 serves as the tunable parameter to map onto the observed temperature function. For the concordance model, Evrard et al. (2002) found $b_T^2 = 1.08 \pm 0.07$ for $\sigma_8 = 0.9$, with a $b_T^2 \propto \sigma_8^{-5/3}$ scaling driven by the behavior of the tail of the mass function. We generalize this result to nonconcordance models by replacing σ_8 with S_8.

Before comparing this result with the range allowed by gas dynamic simulations, we need to apply a correction to account for the radial scale of X-ray temperature measurements. We have calibrated the virial relation at $\Delta = 200$, but the observed values of $T_{\rm X}$ are derived from photons that sample regions interior to this. The exact regions sampled depend on the observing conditions, but high-quality data typically extend to r_{500} (Pratt et al. 2006).

We thus apply a correction factor to b_T^2 that aligns the dark matter velocity dispersion to r_{500}. We use a factor $\sigma^2_{\rm DM}(<r_{200})/\sigma^2_{\rm DM}(<r_{500}) = 0.84 \pm 0.06$, where the central value assumes an NFW profile with concentration[14] $c_{200} = 4.8$ (Dolag et al. 2004), and the quoted error reflects varying the concentration between values of 3 and 15.

The scale-aligned value of the specific thermal energy ratio that matches the local temperature function is

$$b_T^2\big|_{r_{500}} = (0.77 \pm 0.07) S_8^{-5/3}. \quad (17)$$

This temperature function constraint equivalently sets the zero point of the mass-temperature relation

$$\langle M_{500}(6\ {\rm keV})\rangle = (0.54 \pm 0.05) S_8^{5/2} \times 10^{15}\ h^{-1}\ M_\odot. \quad (18)$$

This result, when combined with X-ray observations of the scaling of hot gas mass with temperature, determines the ICM mass fraction at 6 keV. Mohr et al. (1999) measured ICM masses at r_{500} for 45 nearby clusters in an X-ray flux-limited sample. Before forming a mass fraction, we need to align the M_{500} normalization of that work to the value used here. The total mass normalization assumed by Mohr et al. was $M_{500}(6\ {\rm keV}) = 0.46 \times 10^{15}\ h^{-1}\ M_\odot$. Aligning with the mass scale derived from the temperature function, equation (18), requires an increase in mass of 15%, or 5% in linear scale. We use the fact that observed surface brightness profiles indicate a nearly isothermal ICM density profile near r_{500} (Neumann & Arnaud 2001), so the gas mass will scale linearly with radius. We therefore multiply the published result by $1.055\sigma_8^{5/6}$. Note that recent *Chandra* analysis of 11 relaxed clusters indicates that the gas density profile may be somewhat steeper than isothermal, but this affects our correction at the 1% level.

However, we make a second correction for gas asymmetry/clumping that essentially nullifies this 5% increase, while retaining the S_8 scaling. Spherically symmetric models provide an upper limit on the gas mass within a radial shell, as any asymmetries will reduce the amount of gas needed to produce the same emission measure. Simulations show a small degree of gas clumping interior to r_{200} that grows rapidly beyond that radius (Mathiesen et al.

[14] Note that the Dolag et al. (2004) concentration values are quoted against thresholds defined with respect to the background, not critical, density.

1999). Recent ART simulations by Nagai (2006) displayed an overestimate in gas mass of 5% at r_{500}.

Adding 5% additional uncertainty in these corrections, the ICM mass normalization at 6 keV is

$$\langle M_{\rm ICM}(6\ {\rm keV})\rangle = (0.64 \pm 0.05) S_8^{5/6} \times 10^{14}\ h_{70}^{-5/2}\ M_\odot. \quad (19)$$

A potential source of bias that we do not attempt to correct for here is that arising from sample selection. It is likely that local X-ray flux-limited samples are missing the low-luminosity tail of the halo population (Stanek et al. 2006), and this may correspond to the subset with low ICM gas fractions. However, proper modeling of this effect requires that we understand the covariance between $M_{\rm ICM}$, $T_{\rm X}$, and $L_{\rm X}$ for the cluster population. We leave this issue for future work, as it is not a limiting factor in the conclusions drawn below.

With equations (18) and (19), we now form the mean ICM mass fraction at 6 keV based on simultaneously matching the observed temperature function and ICM mass-temperature relation

$$\frac{\langle M_{\rm ICM}\rangle}{\langle M_{500}\rangle} = (0.083 \pm 0.009)\ h_{70}^{-3/2}\ S_8^{-5/3}. \quad (20)$$

We can rewrite this result in terms of the halo baryon fraction and ICM mass fraction, equation (9), and then apply the *WMAP*3 constraint on the global baryon fraction $\Omega_b/\Omega_m = 0.17 \pm 0.01$ (Spergel et al. 2007). This constrains the parameter combination

$$h_{70}^{3/2}\ \hat{f}_{\rm ICM} \Upsilon(6\ {\rm keV}) = (0.49 \pm 0.06) S_8^{-5/3}. \quad (21)$$

We plot this constraint, along with that derived for the specific energy, equation (17), in Figure 13. Bold lines give the central result while thin lines show 90% confidence uncertainties. The horizontal, shaded regions along these curves show the 90% confidence parameter ranges favored by direct simulations, equations (13) and (14) for the X-ray temperature and gas mass fraction, respectively. For the spectroscopic to mass-weighted temperature conversion, we assume $\langle T_{\rm X}/T_m\rangle = 1.10 \pm 0.05$ from Nagai et al. (2006).

The vertical shaded region shows the 90% confidence range of S_8 allowed by the *WMAP*3 and SDSS luminous red galaxy sample analysis of Tegmark et al. (2007). This estimate favors a low-mass normalization for cluster halos, implying high values for the gas specific thermal energy b_T^2 and high values for the hot gas fraction. In fact, the latter must be very close to the cosmic value.

There is significant tension between the low values of b_T^2 seen in simulations and the high values required by the *WMAP*3+SDSS analysis. Even after applying the spectroscopic to mass-weighted correction, an increase of 10%, the gas retains a slightly lower specific thermal energy than the dark matter, $b_T^2 = 0.96 \pm 0.07$. Matching the temperature function in the best-fit *WMAP*3+SDSS cosmology requires $b_T^2 \sim 1.4 \pm 0.2$, nearly a factor 1.5 hotter than current models expect.

Coupled with the galaxy velocity bias discussed above, the low normalization forces the conclusion that current direct simulations are missing 50% of the specific energy in both the hot gas and galaxy components. It is not clear how to modify simulation physics so as to bridge this gap. Since the two components have very different dynamics and thermodynamic behavior, it is likely that two or more independent processes must be invoked.

A higher normalization alleviates much of this tension in energetics. Taking $S_8 = 0.80$ would require only $b_T^2 = 1.1$, a value that lies within 2 σ of the current theoretical expectation. Slightly higher central temperatures, perhaps combined with small errors introduced in the scale alignment argument above, could increase b_T^2 by such a modest amount. The velocity bias parameter would need to be positive, but small, $b_v = 1.05$. Again, this lies within the reach of current direct simulations.

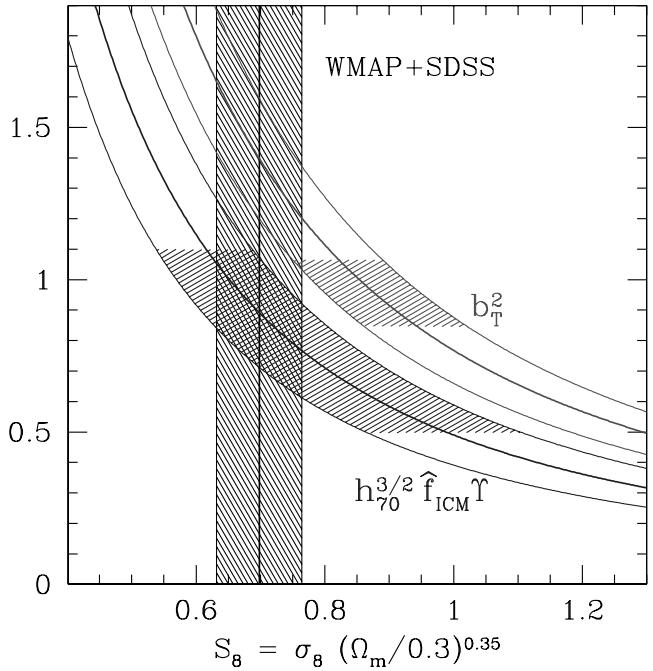

FIG. 13.—Dependence of hot gas thermal energy ratio (*top lines*) and mass fraction (*bottom lines*) on the power spectrum normalization, derived from empirical constraints based on the observed space density of clusters above 6 keV and the observed ICM mass-temperature relation. Shaded regions show expectations for these parameters from direct numerical simulation. The vertical hatched region is a combined *WMAP*3+SDSS constraint on $\sigma_8(\Omega_m/0.3)^{1/2}$ from Tegmark et al. (2007). All regions are shown are 90% confidence intervals. [*See the electronic edition of the Journal for a color version of this figure.*]

4.4. *Discussion*

The above evidence argues for a higher power spectrum normalization, so that the predicted cluster space densities and, to a lesser extent, baryon fractions can match observations without severely taxing direct dynamical simulations. Independent lines of evidence also point to a higher power spectrum normalization. Joint analysis of SDSS, CMB, supernovae, and Lyα forest observations lead to $S_8 = 0.78 \pm 0.03$ (Seljak et al. 2006). Weak gravitational shear measurements in the CTIO lensing survey produce a similar constraint (Jarvis et al. 2006), while combined deep and wide samples of the CFHT Legacy Survey (Semboloni et al. 2006) imply a higher value, $S_8 = 0.89 \pm 0.06$, that reinforces earlier work (Massey et al. 2005).

Pedersen & Dahle (2007) found $S_8 = 0.88 \pm 0.09$ from weak-lensing mass determinations of a local ensemble of 30 X-ray–selected clusters with temperatures near 8 keV. However, subsequent analysis by Dahle (2006) of a slightly extended sample revised this value substantially downward, to $S_8 = 0.67^{+0.04}_{-0.05}$. Uncertainty in mean cluster masses is also apparent in recent studies of the scaling of X-ray luminosity with total mass. While Stanek et al. (2006) favored a high $S_8 \sim 0.8$–0.9 coupled with a substantial level of intrinsic scatter in mass at fixed luminosity, $\sigma_{\ln M} \simeq 0.25$–$0.4$, an alternative perspective of $S_8 = 0.7$ with essentially no scatter is advocated by Reiprich (2006). It is worth keeping in

mind that the difference in halo mass between $S_8 = 0.7$ and 0.9 is substantial, a factor of 2 at $10^{-6.5}\ h^3\ \mathrm{Mpc}^{-3}$ space density (Fig. 12).

The *WMAP*3+SDSS normalization implies that the hot ICM mass fraction within r_{500} is 10% lower than the cosmic baryon-to-total ratio, a value consistent with previous studies (Allen et al. 2004). Higher normalizations require this fraction to be lower. For $S_8 = 0.8$, the value is $(0.71 \pm 0.09)\ h_{70}^{-3/2}$. Recent evidence for lower gas fractions comes from interferometric observations of the Sunyaev-Zel'dovich effect in a sample of 38 clusters (LaRoque et al. 2006), from analysis of CMB distortions induced by nearby clusters (Afshordi et al. 2005, 2007) and from *Chandra* X-ray observations of relaxed clusters (Vikhlinin et al. 2006). Higher normalizations may run into difficulties with gas depletion being too large. A concordance model, $S_8 = 0.9$, implies an ICM fraction of $0.58\ h_{70}^{-3/2}\ \Omega_b/\Omega_m$ within r_{500}. Such a low value requires a higher star formation efficiency, which would be difficult to reconcile with optical observation, or larger baryon losses, perhaps driven by AGN feedback.

Our analysis of the space density as a function of galaxy velocity dispersion reaches the same conclusions as Rines et al. (2006), but our approaches differ. Their analysis is based on virial mass estimates that are assumed to be unbiased. They conclude that a third-year *WMAP* value of S_8 requires a substantial velocity bias $b_v = 1.30 \pm 0.05$, a result that agrees well with our Figure 12. The fact that this loop closes supports the assumption that properly applied virial mass estimators are not strongly biased (see Biviano et al. 2006, and references therein).

Finally, we note that the common $S_8^{-5/3}$ scaling of both the gas temperature and the ICM mass fraction is in apparent contradiction with expectations from simple physical models for cluster structure (Ostriker et al. 2005). Within a given potential, one would anticipate an anticorrelation between T_X and f_{ICM}, since gas heated above the virial temperature would tend to expand and thereby reduce the local gas mass fraction. The scalings derived here from statistical arguments must ultimately be reconciled with physical models based on detailed observations of clusters at X-ray, optical, and submillimeter wavelengths.

5. CONCLUSIONS

We present a precise calibration of the virial scaling for massive dark matter halos derived from an ensemble of large-scale structure simulations. The large majority (∼90%) of halos more massive than $10^{14}\ h^{-1}\ M_\odot$ comprise a regular population that obeys a power-law virial relation between one-dimensional velocity dispersion σ_{DM} and mass, with self-similar slope 0.3361 ± 0.0026 and lognormal scatter $\sigma_{\ln\sigma} = 0.0426 \pm 0.0015$. The value of the intercept at $h(z)M_{200} = 10^{15}\ M_\odot$ is 1082.9 ± 4.0 km s^{-1}. The remaining ∼10% of the population are smaller members of merging systems (satellite objects) that display an elevated mean and dispersion. Our study uses a very simple approach for defining satellites, and we anticipate further improvements in understanding this minority population with a more refined halo treatment. The virial relation is consistent across six cosmological codes and, within the finite range sampled, appears insensitive to assumed cosmology or the presence of a trace amount of dissipationless baryons. Future work should address the robustness of this result to the inclusion of gas that is allowed to cool, dissipate, and form stars.

Combining this relation with a precise determination of the mass function enables detailed predictions for the space density of halos as a function of their internal specific energy. Introducing dimensionless ratios to describe baryon component specific energies, we apply these space density predictions to observations of galaxy velocity dispersion and X-ray temperature. We find that a low normalization cosmology, $\sigma_8(\Omega_m/0.3)^{0.35} = 0.69$, suggested by *WMAP*3+SDSS analysis requires an increase, by a factor 1.5, in values of T_X and σ^2_{gal} expected from the current generation of direct structure formation simulations. A higher normalization, $S_8 = 0.80$, alleviates this tension and implies that hot baryon fractions within r_{500} that are consistent with estimates from current X-ray and Sunyaev-Zel'dovich observations. Even larger values of the power spectrum normalization would require substantial loss of baryons within massive clusters.

We thank the referee for valuable suggestions on the original manuscript. This work was supported in part by NASA grant NAG5-13378 and by NSF ITR grant ACI-0121671. A. E. thanks the Miller Foundation for Basic Research in Science at the University of California, Berkeley, the Japan Society for Promotion of Science for support, and Takako Horikawa for work at the early stages of this project. Some of the simulations in this paper were realized by the Virgo Supercomputing Consortium at the Computing Centre of the Max-Planck Society in Garching and at the Edinburgh Parallel Computing Centre. Data are publicly available at http://www.mpa-garching.mpg.de/NumCos. Halo and galaxy data for the Millennium Simulation are publically available at http://www.mpa-garching.mpg.de/millennium.

REFERENCES

Afshordi, N., & Cen, R. 2002, ApJ, 564, 669
Afshordi, N., Lin, Y.-T., Nagai, D., & Sanderson, A. J. R. 2007, MNRAS, 378, 293
Afshordi, N., Lin, Y.-T., & Sanderson, A. J. R. 2005, ApJ, 629, 1
Allen, S. W., Schmidt, R. W., Ebeling, H., Fabian, A. C., & van Speybroeck, L. 2004, MNRAS, 353, 457
Arnaud, M., & Evrard, A. E. 1999, MNRAS, 305, 631
Bahcall, N. A., Ostriker, J. P., Perlmutter, S., & Steinhardt, P. J. 1999, Science, 284, 1481
Becker, M. R., et al. 2007, ApJ, 669, 905
Belsole, E., Sauvageot, J.-L., Pratt, G. W., & Bourdin, H. 2005, Adv. Space Res., 36, 630
Bertschinger, E. 1987, ApJ, 323, L103
Biviano, A., Girardi, M., Giuricin, G., Mardirossian, F., & Mezzetti, M. 1992, ApJ, 396, 35
Biviano, A., Murante, G., Borgani, S., Diaferio, A., Dolag, K., & Girardi, M. 2006, A&A, 456, 23
Borgani, S., et al. 2004, MNRAS, 348, 1078
Bower, R. 1991, MNRAS, 248, 332
Bryan, G. L., & Norman, M. L. 1998, ApJ, 495, 80
Busha, M. T., Evrard, A. E., & Adams, F. C. 2007, ApJ, 665, 1
Busha, M. T., Evrard, A. E., Adams, F. C., & Wechsler, R. H. 2005, MNRAS, 363, L11
Carlberg, R. G., Couchman, H. M. P., & Thomas, P. A. 1990, ApJ, 352, L29
Casertano, S., & Hut, P. 1985, ApJ, 298, 80
Cavaliere, A., & Fusco-Femiano, R. 1976, A&A, 49, 137
Chandrasekhar, S. 1961, Hydrodynamic and Hydromagnetic Stability (Oxford: Clarendon)
Clowe, D., Bradač, M., Gonzalez, A. H., Markevitch, M., Randall, S. W., Jones, C., & Zaritsky, D. 2006, ApJ, 648, L109
Cohn, J. D., & White, M. 2005, Astropart. Phys., 24, 316
Cole, S., & Lacey, C. 1996, MNRAS, 281, 716
Colín, P., Klypin, A. A., & Kravtsov, A. V. 2000, ApJ, 539, 561
Conroy, C., Wechsler, R. H., & Kravtsov, A. V. 2006, ApJ, 647, 201
Cypriano, E. S., Sodré, L. J., Kneib, J.-P., & Campusano, L. E. 2004, ApJ, 613, 95
Dahle, H. 2006, ApJ, 653, 954
De Lucia, G., & Blaizot, J. 2007, MNRAS, 375, 2
de Theije, P. A. M., & Katgert, P. 1999, A&A, 341, 371

Diemand, J., Moore, B., & Stadel, J. 2004a, MNRAS, 352, 535
———. 2004b, MNRAS, 353, 624
Dolag, K., Bartelmann, M., Perrotta, F., Baccigalupi, C., Moscardini, L., Meneghetti, M., & Tormen, G. 2004, A&A, 416, 853
Efstathiou, G., Davis, M., White, S. D. M., & Frenk, C. S. 1985, ApJS, 57, 241
Eke, V. R., Cole, S., & Frenk, C. S. 1996, MNRAS, 282, 263
Ellis, J., Olive, K. A., Santoso, Y., & Spanos, V. C. 2005, Phys. Rev. D, 71, 095007
Ettori, S. 2003, MNRAS, 344, L13
Ettori, S., Dolag, K., Borgani, S., & Murante, G. 2006, MNRAS, 365, 1021
Evrard, A. E. 1990, ApJ, 363, 349
Evrard, A. E., Metzler, C. A., & Navarro, J. F. 1996, ApJ, 469, 494
Evrard, A. E., Summers, F. J., & Davis, M. 1994, ApJ, 422, 11
Evrard, A. E., et al. 2002, ApJ, 573, 7
Faltenbacher, A., & Diemand, J. 2006, MNRAS, 369, 1698
Faltenbacher, A., Kravtsov, A. V., Nagai, D., & Gottlöber, S. 2005, MNRAS, 358, 139
Frenk, C. S., et al. 1999, ApJ, 525, 554
Gao, L., De Lucia, G., White, S. D. M., & Jenkins, A. 2004, MNRAS, 352, L1
Gonzalez, A. H., Zaritsky, D., & Zabludoff, A. I. 2007, ApJ, 666, 147
Gunn, J. E., & Gott, J. R. I. 1972, ApJ, 176, 1
Heitmann, K., Ricker, P. M., Warren, M. S., & Habib, S. 2005, ApJS, 160, 28
Henry, J. P. 2004, ApJ, 609, 603
Henry, J. P., Finoguenov, A., & Briel, U. G. 2004, ApJ, 615, 181
Huterer, D., & White, M. 2002, ApJ, 578, L95
Ikebe, Y., Reiprich, T. H., Böhringer, H., Tanaka, Y., & Kitayama, T. 2002, A&A, 383, 773
Jarvis, M., Jain, B., Bernstein, G., & Dolney, D. 2006, ApJ, 644, 71
Jee, M. J., White, R. L., Benítez, N., Ford, H. C., Blakeslee, J. P., Rosati, P., Demarco, R., & Illingworth, G. D. 2005, ApJ, 618, 46
Jenkins, A., Frenk, C. S., White, S. D. M., Colberg, J. M., Cole, S., Evrard, A. E., Couchman, H. M. P., & Yoshida, N. 2001, MNRAS, 321, 372
Jenkins, A., et al. 1998, ApJ, 499, 20
Kaiser, N. 1986, MNRAS, 222, 323
Kauffmann, G., White, S. D. M., & Guiderdoni, B. 1993, MNRAS, 264, 201
Koester, B. P., et al. 2007, ApJ, 660, 221
Kravtsov, A. V., Nagai, D., & Vikhlinin, A. A. 2005, ApJ, 625, 588
Lahav, O., Lilje, P. B., Primack, J. R., & Rees, M. J. 1991, MNRAS, 251, 128
LaRoque, S. J., Bonamente, M., Carlstrom, J. E., Joy, M. K., Nagai, D., Reese, E. D., & Dawson, K. S. 2006, ApJ, 652, 917
Lima, M., & Hu, W. 2005, Phys. Rev. D, 72, 043006
Lin, Y.-T., Mohr, J. J., & Stanford, S. A. 2004, ApJ, 610, 745
Markevitch, M. 1998, ApJ, 504, 27
Markevitch, M., Gonzalez, A. H., David, L., Vikhlinin, A., Murray, S., Forman, W., Jones, C., & Tucker, W. 2002, ApJ, 567, L27
Massey, R., Refregier, A., Bacon, D. J., Ellis, R., & Brown, M. L. 2005, MNRAS, 359, 1277
Mathiesen, B., Evrard, A. E., & Mohr, J. J. 1999, ApJ, 520, L21
Mohr, J. J., & Evrard, A. E. 1997, ApJ, 491, 38
Mohr, J. J., Mathiesen, B., & Evrard, A. E. 1999, ApJ, 517, 627
Nagai, D. 2006, ApJ, 650, 538
Nagai, D., & Kravtsov, A. V. 2005, ApJ, 618, 557
Nagai, D., Vikhlinin, A., & Kravtsov, A. V. 2007, ApJ, 655, 98
Nagamine, K., & Loeb, A. 2003, NewA, 8, 439
Navarro, J. F., Frenk, C. S., & White, S. D. M. 1995, MNRAS, 275, 720
———. 1997, ApJ, 490, 493
Navarro, J. F., & White, S. D. M. 1994, MNRAS, 267, 401
Navarro, J. F., et al. 2004, MNRAS, 349, 1039
Neumann, D. M., & Arnaud, M. 2001, A&A, 373, L33
O'Hara, T. B., Mohr, J. J., Bialek, J. J., & Evrard, A. E. 2006, ApJ, 639, 64
Ostriker, J. P., Bode, P., & Babul, A. 2005, ApJ, 634, 964
Pearce, F. R., Thomas, P. A., & Couchman, H. M. P. 1994, MNRAS, 268, 953
Pearce, F. R., et al. 1999, ApJ, 521, L99
Pedersen, K., & Dahle, H. 2007, ApJ, in press (astro-ph/0603260)
Peebles, P. J. E. 1970, AJ, 75, 13
———. 1980, The Large-Scale Structure of the Universe (Princeton: Princeton Univ. Press)
Pierpaoli, E., Borgani, S., Scott, D., & White, M. 2003, MNRAS, 342, 163
Popesso, P., Böhringer, H., Brinkmann, J., Voges, W., & York, D. G. 2004, A&A, 423, 449
Prada, F., Klypin, A. A., Simonneau, E., Betancort-Rijo, J., Patiri, S., Gottlöber, S., & Sanchez-Conde, M. A. 2006, ApJ, 645, 1001
Pratt, G. W., Boehringer, H., Croston, J. H., Arnaud, M., Borgani, S., Finoguenov, A., & Temple, R. F. 2007, A&A, 461, 71
Rasia, E., Tormen, G., & Moscardini, L. 2004, MNRAS, 351, 237
Reed, D. S., Bower, R., Frenk, C. S., Jenkins, A., & Theuns, T. 2007, MNRAS, 374, 2
Reiprich, T. H. 2006, A&A, 453, L39
Rines, K., Diaferio, A., & Natarajan, P. 2007, ApJ, 657, 183
Seljak, U., Slosar, A., & McDonald, P. 2006, J. Cosmol. Astropart. Phys., 10, 014
Semboloni, E., et al. 2006, A&A, 452, 51
Shaw, L. D., Weller, J., Ostriker, J. P., & Bode, P. 2006, ApJ, 646, 815
Sheth, R. K., & Tormen, G. 1999, MNRAS, 308, 119
Sirko, E. 2005, ApJ, 634, 728
Smith, G. P., Edge, A. C., Eke, V. R., Nichol, R. C., Smail, I., & Kneib, J.-P. 2003, ApJ, 590, L79
Sodre, L. J., Capelato, H. V., Steiner, J. E., & Mazure, A. 1989, AJ, 97, 1279
Spergel, D. N., et al. 2007, ApJS, 170, 377
Springel, V., White, S. D. M., Tormen, G., & Kauffmann, G. 2001, MNRAS, 328, 726
Springel, V., et al. 2005, Nature, 435, 629
Stanek, R., Evrard, A. E., Böhringer, H., Schuecker, P., & Nord, B. 2006, ApJ, 648, 956
Tegmark, M., et al. 2007, Phys. Rev. D, 74, 123507
Tormen, G., Bouchet, F. R., & White, S. D. M. 1997, MNRAS, 286, 865
Vikhlinin, A., Kravtsov, A., Forman, W., Jones, C., Markevitch, M., Murray, S. S., & Van Speybroeck, L. 2006, ApJ, 640, 691
Voit, G. M. 2005, Rev. Mod. Phys., 77, 207
Warren, M. S., Abazajian, K., Holz, D. E., & Teodoro, L. 2006, ApJ, 646, 881
Weller, J., Ostriker, J. P., Bode, P., & Shaw, L. 2005, MNRAS, 364, 823
White, M. 2002, ApJS, 143, 241
White, M., Hernquist, L., & Springel, V. 2002, ApJ, 579, 16
White, S. D. M., Navarro, J. F., Evrard, A. E., & Frenk, C. S. 1993, Nature, 366, 429
Xue, Y.-J., & Wu, X.-P. 2000, ApJ, 538, 65
Yahil, A., & Vidal, N. V. 1977, ApJ, 214, 347
Zabludoff, A. I., & Zaritsky, D. 1995, ApJ, 447, L21